The effect of galactic contamination on the largest scales in cosmic background radiation maps

Anders Tangvald

The Institute of Theoretical Astrophysics
University of Oslo

Preface

This master thesis was written while a student at the Institute of Theoretical Astrophysics, University of Oslo.
I wish to thank my supervisor Frode K. Hansen for his assistance, motivation and always friendly demeanor. Thanks also to Hans Kristian Eriksen for his assistance in developing the ILC-code, and to my brother Lars Tangvald for proof-reading and general helpful tips along the way.

Anders Tangvald
June 2, 2008

Contents

1 Introduction **3**

2 Background **5**

2.1 Cosmology . . . 5
2.1.1 The Expanding Universe . . . 6
2.1.2 The Big Bang . . . 7
2.1.3 CMB . . . 9
2.1.4 Inflation . . . 10
2.1.5 Foregrounds . . . 11
2.2 Fourier-transforms . . . 12
2.3 Gaussian statistics . . . 17
2.4 Wavelet-transforms . . . 20
2.5 Lagrange multipliers . . . 22
2.6 CMB-Analysis . . . 22
2.6.1 Important terminology . . . 23
2.6.2 COBE . . . 25
2.6.3 WMAP . . . 28
2.6.4 Planck . . . 31
2.6.5 Current results . . . 31
2.7 Physical processes behind foregrounds . . . 32
2.7.1 Synchrotron radiation . . . 33
2.7.2 Thermal dust . . . 35
2.7.3 Free-free emission . . . 35
2.8 Foreground subtraction . . . 36
2.8.1 External Template Fitting . . . 37
2.8.2 Internal Linear Combination . . . 39
2.8.3 WI-FIT . . . 40

3 Algorithm **43**
3.1 Calculation of preferred axis 44
3.2 ETF 44
3.3 ILC 52
3.4 WI-FIT 58

4 Results **63**
4.1 ETF 63
4.2 ILC 75
4.3 WI-FIT 82

5 Discussion **91**
5.1 Future Work 94

List of Figures

2.1 Cosmic Microwave Background 11
2.2 Fourier-transforms 13
2.3 Spherical representation of Y_{lm} 16
2.4 Normal distribution 18
2.5 Mexican-hat wavelet 21
2.6 Power spectrum, without beam or noise 25
2.7 Power spectrum, with beam 26
2.8 Power spectrum, with noise 27
2.9 Mollweide projection, nside=1 28
2.10 WMAP spacecraft 28
2.11 The five WMAP-bands 30
2.12 Multipole alignment 33
2.13 Galactic emission vs. frequency. From [2] 34
2.14 WMAP masks. From [2] 37

4.1 ETF-cleaned V-band using HFF-templates 64
4.2 ETF plots V-band using HFF-templates 65
4.3 ETF-cleaned Q-band with NFG foregrounds 67
4.4 ETF plots Q-band with NFG foregrounds 68
4.5 ETF-cleaned V-band with NFG foregrounds 69
4.6 ETF plots V-band with NFG foregrounds 70
4.7 ETF-cleaned V-band with NFG foreground, large beam 72
4.8 ETF plots V-band with NFG foregrounds, large beam 73
4.9 WMAP cleaned with ETF 74
4.10 ILC-simulations using HFF 76
4.11 ILC plots 77
4.12 ILC-simulations using NFG foregrounds 78
4.13 ILC-simulations, using NFG templates and large beam 80

4.14 ILC-simulations, using NFG templates and large beam 81
4.15 ILC-method, applied to WMAP-data 82
4.16 WIFIT-cleaned V-band, HFF 83
4.17 WIFIT plots V-band, HFF 84
4.18 WIFIT-cleaned V-band, NFG foregrounds 86
4.19 WIFIT plots V-band, NFG foregrounds 87
4.20 Angular distance between quadru- and octopole 89

List of Tables

2.1 WMAP frequencies 29
2.2 Planck frequencies 31

3.1 ETF coefficients 45
3.2 WIFIT templates 61

4.1 ETF mean angular distance, quadrupole, HFF-templates 66
4.2 ETF mean angular distance, octopole, HFF-templates 66
4.3 ETF mean angular distance, quadrupole, NFG foregrounds 71
4.4 ETF mean angular distance, octopole, NFG foregrounds 71
4.5 ETF mean angular distance, quadrupole, large beam 73
4.6 ETF mean angular distance, octopole, large beam 73
4.7 ILC mean angular distance 77
4.8 ILC mean angular distance, NFG foregrounds 78
4.9 ILC mean angular distance, large beam 81
4.10 ILC weights, mean over 500 simulations 82
4.11 WIFIT mean angular distance, quadrupole, HFF 85
4.12 WIFIT mean angular distance, octopole, HFF 85
4.13 WIFIT mean angular distance, quadrupole, NFG foregrounds . . . 88
4.14 WIFIT mean angular distance, octopole, NFG foregrounds 88

Chapter 1

Introduction

The Cosmic Microwave Background (CMB), discovered in 1965, is arguably the strongest evidence in favour of the Big Bang theory. It consists of photons that have travelled freely through space since the era of recombination, and so contains information about the conditions of the early stages of the universe.

The Wilkinson Microwave Anisotropy Probe (WMAP) was launched in 2001 to provide measurements of the CMB. However, these measurements are impaired by several factors, especially the presence of the Milky Way galaxy which obscures our view of the intergalactic space. This sort of contamination is, along with all other non-CMB sources that emit microwave radiation, collectively referred to as *foregrounds*. As the study and measurement of the CMB becomes ever more precise, a more thorough understanding of the nature of these foreground sources becomes vital.
In the study of data from WMAP, some surprising discoveries were made, especially when looking at large-scale structures. In this thesis, we focus on the apparant alignment between two of the largest scales, the *quadrupole* and the *octopole*. These two appear to be orientated along a common axis, in violation of the assumed isotropic nature of the CMB ([27]). In this thesis, 3 different methods of foreground removal are examined and compared in order to check if foreground residuals may be responsible for the alignment—. External Template Fitting (ETF), Internal Linear Combination (ILC) and Wavelet-based hIgh resolution Fitting of Internal Templates (WI-FIT) will be tested in order to determine their effectiveness, and the validity of the properties of the resultant CMB-maps.
Chapter 2 begins with an overview of current theories on the origin of the universe, and a brief introduction to the CMB.

A vital tool in CMB-analysis, the Fourier-transform is discussed in section 2.2, before we discuss Gaussian statistics. Wavelet-transforms and Lagrange multipliers are both used in the algorithm section, these mathematical tools are discussed in sections 2.5 and 2.4.
Then we move on to analyzing the CMB, first introducing some notation and terminology, before giving a short review/preview of past, present and future experiments and results.
The galactic foreground emissions, and the physical processes that drive them is considered next, before the chapter closes with a look at the underlying philosophy behind the three cleaning methods applied in this thesis.

We have used Monte Carlo simulations to implement and test these methods. The details are given in chapter 3.
We have applied the algorithms to both our simulations and the data from WMAP, and the results are presented in chapter 4.
In closing, chapter 5 presents a discussion and comparison of the results achieved by the different methods.

We have found the ILC-method produces the best results, but caution is required. We have worked only with full skymaps, applying ILC and WI-FIT to smaller partitions of the sky can be expected to dramatically improve results.
Regardless, our results seems to imply the alignment between the two multipoles are not foreground-related.

Chapter 2

Background

In this chapter, we lay down the basis for the analysis to come. What is the CMB, and why is it of interest to us? What were the conditions in the early universe like, and what is it's connection to the CMB we observe today?
After trying to answer these questions, we move on to Fourier theory and the related topic of wavelet transforms. Also covered is Lagrangian multipliers and some Gaussian statistics. These are all mathematical tools vital to the algorithms we will be implementing.
Once we have those covered, we can begin with our CMB-analysis. We look at some important terminology, and some of the satellites that have been used, or will be used to observe the CMB, before we close the chapter with a look at foregrounds and ways of removing them from our CMB-maps.

2.1 Cosmology

The information in this chapter is mostly taken from [4], [6] and [16]. The field of astrophysics that deals with the origin and evolution of the Universe as a whole is known as cosmology. It covers topics such as the size, shape and age of the Universe. In order to understand the cosmos today, and predict what it will be like in the future, we need to understand its past. In this thesis, we focus on the Cosmic Microwave Background, leftover radiation from the primordial fireball that filled all space shortly after the event known as the Big Bang. We begin with a look at how the universe is expanding, before moving on to the Big Bang. Then follows an introduction to the CMB.

2.1.1 The Expanding Universe

Two of the most basic questions in cosmology are how big is the universe, and has it always been this size? At the time of Isaac Newton, the universe was imagined to be infinite and static. In such a model, the universe is infinitely old, will exist forever and is filled with an infinite amount of stars. However, this model raised a dilemma: Why is the night sky dark? If there are an endless amount of stars and the universe in infinitely old, there should be a star along every line of sight. This is known as *Olbers paradox*, named after the astronomer who first noticed the problem.

When Einstein formulated his theory of relativity, he found that it did not describe a static universe, but rather one that is expanding. Though Einstein did not trust his own conclusions on this matter initially, the discoveries of Edwin Hubble confirmed that the universe was indeed growing in size. Vesto Slipher had earlier discovered that the majority of galaxies were moving away from us, by noting that their spectral lines were shifted towards the red end of the spectrum, a phenomenon known as *redshift* [34]. By studying the spectra of distant galaxies, Hubble found there was simple linear relationship between the distance from Earth and the *recessional velocity*, the speed with which the galaxy is moving away from us.

This relationship is known as **Hubble's law**,

$$v = H_0 d \tag{2.1}$$

where v is the velocity, d is the distance and H_0 is known as Hubble's constant. The 0-subscript indicates present time. The redshift z of a given object is found through the relation

$$z = \frac{\lambda - \lambda_0}{\lambda_0} = \frac{\Delta\lambda}{\lambda_0} \tag{2.2}$$

λ is the wavelength found in the spectrum being analyzed, λ_0 is the ordinary, unshifted wavelength that line would be found at in a stationary object.

The true value of Hubble's constant is still a hot topic in cosmology. It expresses the rate at which the Universe is expanding, and can be used to calculate the age of the Universe. Analysis of the WMAP-data has given a current value of $H_0 = 70.1 \pm 1.3\, km/s/Mpc$ [18].

A way of quantifying the distance between us and other galaxies is through the *scale factor*. It is typically identified by a lower-case *a*, and is the ratio between the current size of the universe to the size at some point in the past. It is defined to be equal to one at present time, and hence it must have been smaller than one at any

time in the past assuming an continuously expanding Universe. Understanding how a changes with time is critical to understanding the history and evolution of the universe up until today. It is currently believed that $a \propto t^{\frac{2}{3}}$, t being time [6], under the assumption that the universe is flat and matter-dominated.
The scale factor is linked to the Hubble constant through the **Hubble rate**,

$$H_t = \frac{da/dt}{a} \tag{2.3}$$

The Hubble constant is then the Hubble rate today($t = 0$).
The photons that comprise the CMB will have experienced stretching as they travel through the cosmos due to the expansion of space. The temperature of the photon that comprise the CMB today is roughly 2.75 Kelvin. Since the energy of a photon is inversely proportional to its wavelength, the wavelength at some time in the past would have been smaller by a factor of $1/a$. This leads to the temperature function

$$T(t) = \frac{T_0}{a(t)} \tag{2.4}$$

where T is the temperature of the CMB [6].

2.1.2 The Big Bang

The motion of the galaxies as they move along with the expansion of space is known as the **Hubble flow**. It shows that the Universe has been expanding for billions of years, which implies that the Universe must have been smaller and denser in the past than what it is today. A logical consequence of this is if we look far enough back through time, there must have been a time when the density was infinitely high and concentrated in a very small space. The point in time when the Universe begun expanding from this state is known as the Big Bang. Using the Hubble constant, we can estimate the time t_0 that has passed since this event by calculating how long it would take for two galaxies, separated by d, to collide while travelling at the relative velocity v

$$t_0 = \frac{d}{v} \tag{2.5}$$

Inserting Hubble's law, $v = H_0 d$, we get

$$t_0 = \frac{1}{H_0} \tag{2.6}$$

With the value for H_0 quoted above, this leads to a value for t_0 of approximately 14 billion years. This is however only an estimate, as the above assumes the universe has been expanding at a constant rate, which is in all likelihood an incorrect assumption.
With a finite age of the universe, Olber's paradox is also resolved. Starlight from stars that lie more than 14 billion light-years away have not reached us yet, they are in effect invisible to us.

The Early Universe

Immediately after the Big Bang, the universe was extremely dense and hot. In such an environment, atoms were unable to form due to the constant violent collisions between particles. The study of the early universe is then intimately tied to elementary particle physics. An important concept of this is the *Heisenberg uncertainty principle*, which states that there is a mutual uncertainty between position and momentum. In other words, a higher accuracy in the measurement of a particle's position leads to a higher uncertainty in the measurements of the particle's momentum. An analoguos principle states that the relationship between the energy of a system and time is equally uncertain. Since energy is linked to mass through the famous $E = mc^2$, we can not be sure over a brief time interval how much matter there is in a given location. During this brief time interval, matter can then appear and disappear. The particles created come in pairs, of matter and antimatter. They are identical in all aspects except for their electric charges having opposing signs. These pairs of particles are known as *virtual pairs*, since they can not be directly observed.
These particles usually annihilate themselves by colliding with each other, producing radiation.

The creation of pairs of matter and anti-matter particles can become *real* however. Photons with a very high energy, can interact with each other, and the result will be a pair of particle and antiparticle. With higher energy-photons comes the production of more massive particles. As the universe expanded, it also cooled. The photons lost energy, and the more massive particles could no longer be created.
After about 1 second, the temperature was too low for any particles to be created, however the annihilation process continued, decreasing the matter content and fill-

ing space with radiation. As all we see in the universe today is made of matter, there must have been a surplus of matter over antimatter in the early stages of the universe.
The universe we observe today contains mostly hydrogen and helium. This fact, together with the observed expansion of space is powerful and compelling evidence in favour of the Big Bang theory. A third piece of convincing evidence is the Cosmic Microwave Background(CMB).

2.1.3 CMB

Since the early universe was so hot, it must have been filled with high-energy photons. Given the high density, the *mean free path* of those photons will have been so short as to ensure the cosmic radiation field would be kept at thermal equilibrium. Under such conditions, the radiation would have a blackbody spectrum.
This property means we can calculate the temperature of the radiation field at some time in the past using **Wien's law**

$$\lambda_{max} T = 0.29 cmK \tag{2.7}$$

where λ_{max} is the peak wavelength and T is the temperature. This law states that the wavelength is inversely proportional to the temperature. Using this, we can state the temperature of the CMB radiation at some time T_t in the past as a function of redshift

$$T_t = z * 2.7K \tag{2.8}$$

In the early, hot universe, elementary particles were unable to form atoms due to the high-energy photons that filled space. Instead, the universe was filled with an opaque soup of protons, electrons and photons. The highest temperature which allows hydrogen-atoms to form is about 3000 K. Using Wien's law, this means the first atoms were formed about 270,000 years after the Big Bang, at a redshift of $z \approx 1000$. This time is called the **era of recombination**, referring to electrons and protons combining to form atoms. Despite the name, these particles had never before combined into atoms.
The hydrogen atom does not absorb low-energy photons, and these were therefore free to escape into space. The universe became transparent. These photons have travelled freely through space since, and form what we call the Microwave Background. These photons then form a snapshot of the universe as it was some 300,000 years after the Big Bang, what is known as the last scattering surface.

The CMB is almost perfectly isotropic, it is the same in all directions. High-precision measurements however, do detect slight disturbances around the average temperature of 2.7 K. These small deviations from the isotropy are called anisotropies. The temperature-drop from 3000 K at the era of recombination to today's 2.7 K is caused by the expansion of space, which stretches the photons causing them to lose energy.
The CMB perturbations were caused by the last scattering surface not being entirely uniform. Why it was not uniform will be discussed in section 2.1.4.
Gravitational attraction led matter to be clumped in some places, while other areas had correspondingly less matter. In the areas were there was an excess of matter, the gravitational potential would be lower. This would cause the photon, as they escaped the primordial soup to be stretched, or redshifted, as they escaped these gravitational wells. Similarly, photons leaving areas that were less dense than the average, would be blueshifted.
In addition to this, interaction with matter after the photons left the surface of last scattering also affects their wavelength. As a photon approaches a concentration of mass, it is blueshifted. Once past, it is redshifted. These two will cancel each other out, unless the gravitational field undergoes some change during the transit. The processes that produce new perturbations to the photons are known collectively as the *integrated Sachs-Wolfe effect*. [6]
Figure 2.1 shows a map of the CMB perturbations around the mean 2.7 K, based on data from the WMAP-satellite.

2.1.4 Inflation

The statistical properties found in the CMB raises a problem. Why is it the same all over the sky? Given the finite age of the universe and the speed of light, we have two constraints as to how far information can possibly have travelled. Yet areas separated by even larger distances have almost exactly the same temperature to an accuracy of 1 in 10,000. This is known as the **horizon problem**.
A suggested solution lies in the theory of Inflation. This proposes that in its very early stages, the universe went through a short period of rapid expansion, called the **inflationary epoch**. Thus, two points in the sky that was originally near each other, were moved apart by enormous distances.
This not only answers the question of why the CMB is so uniform, but also why it is not *completely* uniform. Heisenbergs uncertainty principle guarantees that the early, pre-inflation universe can not have been perfectly smooth. There would have been tiny, quantum fluctuations that, through the sudden onset of explosive

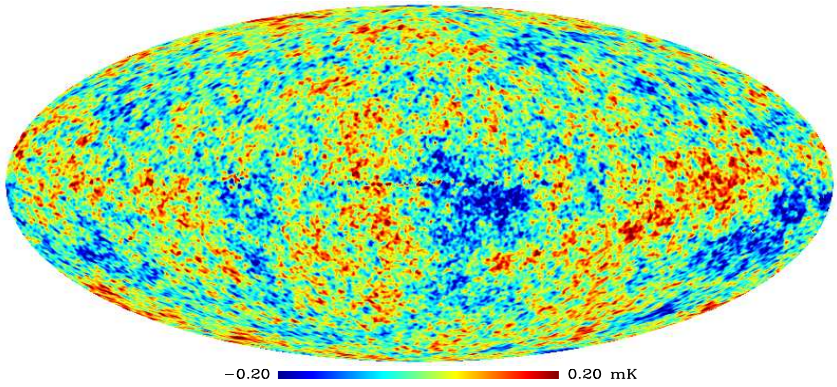

Figure 2.1: Cosmic Microwave Background, from WMAP, cleaned with ILC-algorithm

inflation, would have grown to the scales we observe in the CMB-fluctuations today [9]. The processes that would drive inflation are not very well understood, but there are several predictions made that can be tested by observing the CMB. As already explained, the isotropy of the universe is one such prediction. The universe should look the same in all directions.
Following on from this, inflation predicts the CMB fluctuations should follow a Gaussian distribution 2.3, and that the CMB should show B-mode polarization. Investigating whether this is acually the case is therefore of vital importance to determining the accuracy of inflation-theory.

2.1.5 Foregrounds

Whilst the Milky Way provides a spectacular sight on clear nights, it is also one of the greatest obstacles we face in the study of the cosmos. Observing any object or phenomena usually requires a clear line of sight, and the CMB is no different. The galaxy emits radiation in the same microwave frequency range as we find the CMB, and thus obscures the background radiation. As changing our vantage point

is not a viable option, overcoming this problem becomes vital in order to produce results that yield credible information about our universe.
The galactic emission is mainly a product of three separate physical processes,

- Synchrotron radiation
- Thermal dust emission
- Free-Free emission

These will be covered in section 2.7.

Though the term foregrounds chiefly refers to galactic emission sources, it also applies to anything that might obscure our view of the CMB, including extra-galactic sources.
The correct treatment of foreground-signals is absolutely vital to accurate analysis of the CMB and its properties.

2.2 Fourier-transforms

Analyzing CMB-maps can be a time-consuming and computationally demanding excercise. It is therefore important to explore ways of reducing the workload, and to find mathematical tools to lessen the demands on computer power. The Fourier series and its extension, the Fourier transform do just that. First introduced by Jean Baptiste Fourier, the underlying principle can easily be formulated: Any periodic function can be described as a sum of sines and cosines, each multiplied by different coefficients. The concept is illustrated in figure 2.2, splitting the original, complex signal with no apparant periodicity into several smaller, periodic sinusoids.
Using Euler's formula,

$$e^{i\theta} = cos(\theta) + i\, sin(\theta) \tag{2.9}$$

the series itself has the form

$$f(x) = \sum_{n=-\infty}^{\infty} c_n e^{\frac{2\pi n}{T} ix} \tag{2.10}$$

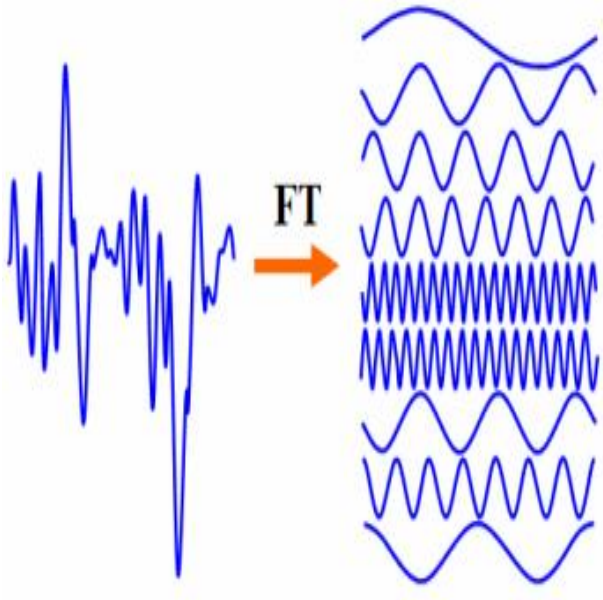

Figure 2.2: Fourier-transforms

where $f(x)$ is a periodic function with period T, and

$$c_n = \frac{1}{T}\int_{-T/2}^{T/2} f(x)e^{-\frac{2\pi n}{T}ix}dt \tag{2.11}$$

In order for a function to be expressed as a Fourier-series, it must satisfy the following conditions, [31]

- The function is periodic
- It it continuous and single-valued
- A finite number of extrema within one period
- The integral must converge

What then about functions that are not periodic, such as the CMB? This brings us to the Fourier transform, which provides a representation of functions that have no particular periodicity. The term transform refers to the original function being transformed into a new representation that exists in the frequency domain, where it is easier to manipulate the transformed function.

The transform(in one dimension) is defined by

$$\tilde{f}(k) = \int_{-\infty}^{\infty} f(x) e^{-i2\pi kx} dx \tag{2.12}$$

The reverse transform, from the frequency domain back to pixel-space is given by

$$f(x) = \int_{-\infty}^{\infty} \tilde{f}(k) e^{i2\pi kx} dk \tag{2.13}$$

$f(x)$ here represents the original function in discrete space, $\tilde{f}(k)$ is the transformed function in the frequency domain [19]. Both these operations(eqs. 2.12 and 2.13) share an important property, that a function can be recovered completely after a transform via the inverse process. This means no information is lost as we move back and forth between pixelspace and the frequency domain.

Extending the concept into two dimensions, the transform is now defined by

$$\tilde{f}(k_x, k_y) = \int_{-\infty}^{\infty} f(x, y) e^{-i2\pi(k_x x + k_y y)} dx dy \tag{2.14}$$

and the reverse

$$f(x, y) = \int_{-\infty}^{\infty} \tilde{f}(k_x, k_y) e^{i2\pi(k_x x + k_y y)} dk_x dk_y \tag{2.15}$$

where x and y as used in the context of this paper are spatial coordinates referring to a specific pixel in a map. k_x and k_y defines the continuous frequency domain as in the one-dimensional case.
However, the CMB-signal is not represented as a continuous function, but rather as a set of discrete pixel-values. By substituting the discrete function f_n for the continuous f(x) in equations 2.12 and 2.13, an expression for the Discrete Fourier Transform (DFT) can be found,

$$\tilde{f}(k) = \sum_{n=0}^{M-1} f(x) e^{\frac{-i2\pi}{M} kx} \tag{2.16}$$

Even though f_n is a discrete function, its Fourier-representation is continuous. The reverse transform is as follows

$$f(x) = \frac{1}{M} \sum_{k=0}^{M-1} \tilde{(f)}(k) e^{\frac{i2\pi}{M} kx} \tag{2.17}$$

Extending once again to two dimensions, the transforms are given by the following equations,

$$\tilde{f}(u,v) = \sum_{x=0}^{M-1}\sum_{y=0}^{N-1} f(x,y)e^{-i2\pi(ux/M+vy/N)} \tag{2.18}$$

$$f(x,y) = \frac{1}{MN}\sum_{u=0}^{M-1}\sum_{v=0}^{N-1} \tilde{(}f)(u,v)e^{i2\pi(ux/M+vy/N)} \tag{2.19}$$

Finally, the concept can be extended to a spherical surface through what is known as spherical harmonics. Spherical harmonics refers to the angular part of the solution to the Laplace's equation($\nabla^2\varphi = 0$) in spherical coordinates, and are given by,

$$Y_{lm}(\theta,\phi) = (-1)^m \left[\frac{2l+1(l-m)!}{4\pi(l+m)!}\right] P_l^m(cos\theta)e^{im\phi} \tag{2.20}$$

with $m \geq 0$. Y_{lm} is known as a spherical harmonic function of degree l and order m. l and m are both integers, with $m = -l, -(l-1), -(l-2), ..., 0, ..(l-1), l$ and are analogous to the Fourier-variables k_x and k_y. θ and ϕ are spherical coordinates, similar to the cartesian coordinates x and y uses in the Fourier transforms above. P_l^m is the associated Legendre polynomial.
For values of $m < 0$, the spherical harmonic is

$$Y_l^m(\theta,\phi) = (-1)^{|m|}\left[Y_l^{|m|}(\theta,\phi)\right]^* \tag{2.21}$$

with the asterisk representing complex conjugation.
The CMB temperature field $T(\theta,\phi)$ can then be expanded as a sum of spherical harmonic functions,

$$T(\theta,\phi) = \sum_{l=0}^{\infty}\sum_{m=-l}^{l} a_{lm}Y_l^m(\theta,\phi) \tag{2.22}$$

where the coefficients a_{lm} are given by

$$a_{lm} = \int_{-1}^{1}\int_{0}^{2\pi} T(\theta,\phi)Y_{lm}(\theta,\phi)d(cos\theta)d\phi \tag{2.23}$$

Equation 2.22 is an exact analogy with a Fourier series. Just as in the Fourier-case, no information is lost in the transform from the temperature field $T(\theta,\phi)$

to the a_{lm}-constants. Figure 2.3 visualizes the spherical harmonics-function Y_{lm} for different values of l and m. The function changes sign each time it crosses one of the longitudinal or latitudinal lines, and has a value of zero on the lines themselves. As the figure indicates, l can be interpreted as being related to the size of structures in the CMB-field, while m denotes position on the sphere.

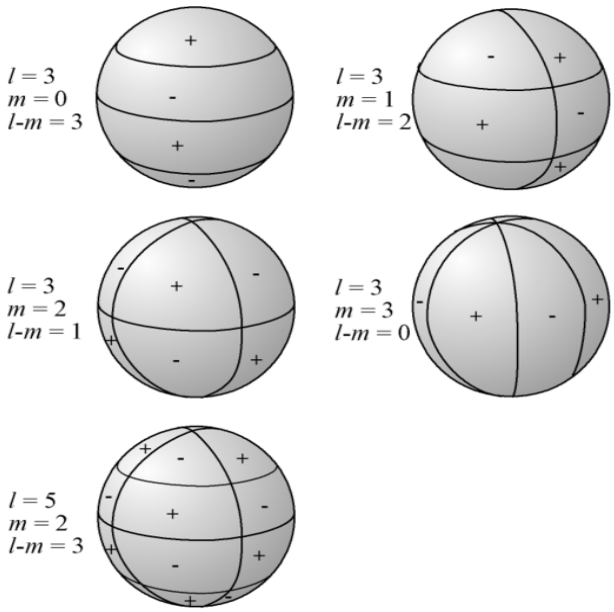

Figure 2.3: Spherical representation of Y_{lm}. From http://www.wikipedia.org

2.3 Gaussian statistics

One of the most central assumptions about the background radiation is that it follows what is known as a Gaussian, or normal, probability distribution. This means, we can expect statistical properties of the CMB measurements to follow certain rules, such as the value of the $mean$ and $variance$.
The mean is simply the average of the values in a given population of sampled measurements. Thus, the mean of value x from N samples is

$$\langle x \rangle = (x_1 + x_2 + x_3 + ... + x_N)/N \tag{2.24}$$

Another key concept is the standard deviation, a commonly used measure of the spread in population values,

$$\sigma = \sqrt{\frac{(x_1 - \langle x \rangle)^2 + ... + (x_N - \langle x \rangle)^2}{N - 1}} \tag{2.25}$$

Following on from this, we can define the variance σ^2, another commonly used measure.

The normal distribution is defined by

$$P(x) = \frac{1}{\sigma\sqrt{2\pi}} e^{-\frac{(x-\mu)^2}{2\sigma^2}} \tag{2.26}$$

where μ is the mean and σ is the standard deviation. It is displayed in figure 2.4, showing how the curve will respond to some different mean and variance-values.
As the figure shows, samples are spread symmetrically about the mean, with the probability of large deviations dropping quickly towards zero.
Thia can be formalized with the *68-95-99.7-rule*. This tells us approximately 68% of the samples in a normally distributed population will fall within 1σ of the mean μ, 95% within 2σ and 99.7% within 3σ. The "standard normal distribution" is defined as $\mu = 0$ and $\sigma^2 = 1$ [36].

One property of this figure which will become important later on is what is called the FullWidth Half-Maximum(FWHM). It is the width of the curve at half the maximum value. For a normal distribution, this is related to the standard deviation by,

$$\sigma = \frac{FWHM}{\sqrt{8ln2}} \tag{2.27}$$

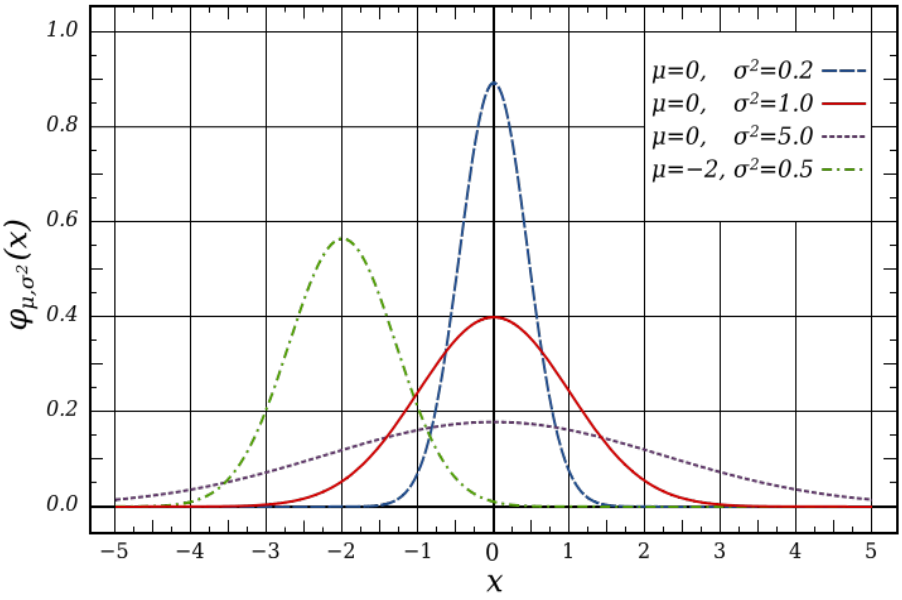

Figure 2.4: Normal distribution, from http://www.wikipedia.org

We know the measured anisotropy-distribution in one spot is strongly linked to the values in other spots. A positive or negative value in one location will tend to influence the value in neighbouring spots in the same positive or negative direction. This phenomenon can be summarized by the terms covariance and correlation. Covariance is a measure of the strength of the relationship between two values x_1 and x_2 and is quantified as

$$cov(x_1, x_2) = \langle (x_1 - \mu_1)(x_2 - \mu_2) \rangle \tag{2.28}$$

with μ_1 being the mean for variable x_1 and μ_2 the mean for x_2. The relationship between two such values is called correlation, a measure of how the value of x_1 depends on the value of x_2, and can be expressed as

$$corr(x_1, x_2) = \frac{cov(x_1, x_2)}{\sigma_1 \sigma_2} = \frac{\langle (x_1 - \mu_1)(x_2 - \mu_2) \rangle}{\sigma_1 \sigma_2} \tag{2.29}$$

where σ_1 is the standard deviation of x_1, σ_2 of x_2.
Using these two definitions, the correlation and covariance matrices can be constructed by expanding the above equations to n dimensions.

The covariance matrix is then

$$Cov_{ij} = \langle (x_i - \mu_i)(x_j - \mu_j) \rangle \tag{2.30}$$

and the correlation matrix

$$Corr_{ij} = \frac{\langle (x_i - \mu_i)(x_j - \mu_j) \rangle}{\sigma_i \sigma_j} \tag{2.31}$$

Obviously, these two matrices are both symmetric.

The usefulness of the Fourier transform is shown by applying the above two concepts to a transformed function. For the applications described in this thesis, a correlation matrix is a NxN-matrix, with $N \approx 3million$. Due to time-considerations, working with such matrices is not viable. The correlation between two Fourier-modes k and k'

$$\left\langle \tilde{f}(k)\tilde{f}(k') \right\rangle \tag{2.32}$$

$\tilde{f}(k)$ being defined by 2.12, can be found by making use of

$$\int e^{ik(x'-x)} dx = \delta^D(x' - x) \tag{2.33}$$

where δ^D is the Dirac δ-function

$$\delta^D(t) = \begin{cases} 1 & \text{t} = 0 \\ 0 & \text{otherwise} \end{cases} \tag{2.34}$$

This results in

$$\left\langle \tilde{f}(k)\tilde{f}(k') \right\rangle = \delta^D(k' - k) \int \int C(x' - x) e^{-ik'(x'-x)} \, dx dx' \tag{2.35}$$

The integral, where C is a correlation-function, is called the power-spectrum. This will be explained further in chapter 2.6. What the above result tells us is that two Fourier-modes are correlated only if $\delta^D(k' - k) \neq 0$, which is only true if $k' = k$. Thus, there is no correlation between different modes in Fourier-space.

2.4 Wavelet-transforms

Earlier, we saw that a function can be restated as a sum of sinusoids. We used this property to derive the Fourier-transform. However, this transformation has limited power, because the transformed function accurately represents frequency resolution, but scale and time resolution are poorly approximated. Though all frequencies present in a signal may be known, we cannot determine when or where they are present.

Attempts to overcome this problem falls within the field of *multi-resolution theory*, which is concerned with the analysis of functions or signals at more than one resolution.

The basic idea is to cut the signal or function of interest into several smaller parts, and study them separately. *Wavelets* are one way of such a dividing up of a signal, using a scalable, sliding window to split it into parts than can then be analyzed individually.

The wavelets themselves are formed from what is known as the *mother wavelet*, by scaling and translation

$$\Psi_{s,\tau}(x) = \frac{1}{\sqrt{s}}\Psi\left[\frac{x-\tau}{s}\right] \tag{2.36}$$

where s and τ are called the scale and translation parameters, respectively. Using this definition, we can write the continuous wavelet transform in one dimension as

$$\gamma(s,\tau) = \int_{-\infty}^{\infty} f(x)\Psi_{s,\tau}(x)\,dx \tag{2.37}$$

The similarity with Fourier transforms should be obvious, the only difference being the nature of the *basis function*, with wavelets replacing sinusoids. However, there is one important change, the wavelets themselves are not specified. They can be designed and molded to fit one's wished and needs in each separate case. The inverse transform is given by

$$f(x) = \frac{1}{C_\Psi}\int_0^{\infty}\int_{-\infty}^{\infty}\gamma(s,\tau)\frac{\Psi_{s,\tau}(x)}{s^2}\,d\tau\,ds \tag{2.38}$$

where

$$C_\Psi = \int_{-\infty}^{\infty}\frac{|\psi(k)^2|}{|k|}\,dk \tag{2.39}$$

where $\psi(k)$ is the Fourier transform of $\Psi(x)$. As long as the *admissibility criterion* $C_\Psi < \infty$ is satisfied, the wavelets can be used to analyze and then reconstruct the

original function through the two equations above. This condition also tells us that $\psi(0) = 0$ and that the average value of the wavelet is zero,

$$\int_{-\infty}^{\infty} \Psi(x)\, dx = 0 \tag{2.40}$$

In other words, $\Psi(x)$ must be a wave.

Specifically as applied to this thesis, the wavelets used are what are known as Spherical Mexican Hat wavelets. They are proportional to the second derivate of a Gaussian distribution(equation 2.26):

$$\Psi(x) = \left(\frac{2}{\sqrt{3}}\pi^{-\frac{1}{4}}\right)(1 - x^2)e^{-\frac{1}{2}x^2} \tag{2.41}$$

Its name is derived from it's distinctive shape, shown in figure 2.5 [28] has shown

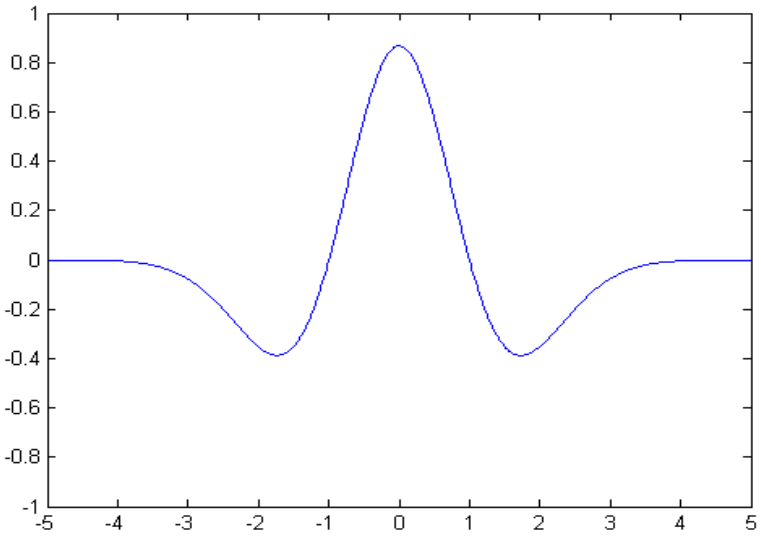

Figure 2.5: Mexican-hat wavelet

the Spherical Mexican Hat wavelets to be very effective for the analysis of non-Gaussian features in the CMB.

2.5 Lagrange multipliers

A common problem in calculus is finding the maxima and minima points, collectively known as extrema, for a given function. A typical complication arises when the function is constrained by one or more outside conditions.
Lagrange multipliers is en excellent tool when it comes to finding the extrema of a multi-variate function when there are such constraints.
Assume a function $f(x_1, x_2)$ for which we wish to find the maxima or minima, subject to the constraint $g(x_1, x_2) = d$, for some value of d.
Lagrangian multipliers uses the fact that in any extrema within the area bounded by $g(x_1, x_2)$, the gradient of $f(x_1, x_2)$ must run parallell to the gradient of $g(x_1, x_2)$, the gradient being a vector perpendicular to the function and pointing towards the direction in which the function is growing the fastest.
Formalizing this condition, we can write,

$$\nabla f(x_1, x_2) = \lambda \nabla g(x_1, x_2) \tag{2.42}$$

If the two gradients line up, one is a multiple of the other by the constant λ. This equation can be expanded as

$$\frac{\partial f}{\partial x_k} = \lambda \frac{\partial g}{\partial x_k} \tag{2.43}$$

where $k = 1, 2...n$ for n variables.
This is a system of $n + 1$ equations(including the constraint $g(x_1, x_2) = d$) with $n + 1$ unknowns, that can be solved to find the extremum points.

2.6 CMB-Analysis

The existence of the CMB was first predicted in the 1940's, as a natural consequence of the Big Bang theory. In a famous article, Ralpha Alpher and George Gamow outlined how the abundance of hydrogen and helium could be explained by a Big Bang model of the universe [1]. This paper also predicted there should be radiation left over from the intense heat of the early universe, that should now hold a temperature of about 5K [4].
20 years later, the CMB-radiation was detected when two radio-astronomers found an excess signal they could not otherwise account for [30]. Moving on from accidental discoveries, the field of CMB-analysis is now a rich field for study of the conditions of the early universe.

In this section, we will introduce some basic terms and ideas involved in this analysis, then discuss some past and future experiments to study the CMB, before talking about some of the most important discoveries that has resulted from these experiments.

2.6.1 Important terminology

When observing the sky, a telescope can not observe an arbitrarily small section of the sky, rather the resolution is determined by the size of the *beam*. When observing a point in the sky, the telescope is actually observing not only that point, but also the surrounding area, the size of that area being determined by the *resolution* of the beam.
The temperature assigned to the central point is then a weighted contribution from the entire area contained within the beam-area, with the weighting being approximately Gaussian.
An actual Gaussian beam has the form

$$B_G = e^{-\frac{\Delta\Theta^2}{2\sigma^2}} \tag{2.44}$$

and in spherical harmonics space

$$B_G = e^{-(\sigma^2 \times l \times (l+1)/2)} \tag{2.45}$$

where

$$\sigma = \frac{FWHM}{\sqrt{8\,ln\,2}} \tag{2.46}$$

and FWHM is the Full-Width Half Maximum. An associated concept are pixelwindow-functions. Since we can not operate with maps with an infinite amount of pixels, each pixel will cover a certain area of the sky. That pixel will then be assigned a temperature that is an average of the area covered. The actual effect of beams and pixelwindow-functions are that smaller details in the maps will be smeared out.
In equation 2.45, the l's are the same as in equation 2.22 and figure 2.3. As mentioned in the chapter on Fourier-theory, this variable is connected to scale, confirming that the beam serves to suppress smaller scales, since l grows as the scales gets progressively smaller.

The l-coefficients are also known as *multipoles*. A CMB-map contains structures

of several different sizes, or scales. We can then imagine each full skymap as a sum of several other maps, these new maps each containing only structures of a given scale. By multiplying the maps in this new set with a weight(the a_{lm}'s from a spherical harmonic transform), we can recover the original, full map. Each l and m, or multipole corresponds to one such scale-dependent map. How large the set of scale-dependent maps, is determined by a variable known as l_{max}, a small value of this meaning we only look at large scales.
The first few multipoles are called *monopole*($l = 0$), *dipole*($l = 1$), *quadrupole*($l = 2$), and *octopole*($l = 3$). In analysing the temperature variations in the CMB, the monopole is the largest scale, which then is the average temperature across the entire sky, 2.7 K. The dipole, the second largest scale is dominated by a Doppler shift caused by the Earth's movement through the CMB radiation field. Measuring this Doppler-shift, the velocity of our solar system can be calculated. It turns out we are moving through the radiation field at a speed of $371km/s$ [16], but this effect also diminishes our ability to measure the CMB at this scale. Thus, the quadru- and octopole are the largest scales where CMB-anisotropies can be observed.

A vital statistic about the CMB-anisotropies is of course how much they deviate from the mean, in other words the variance. In spherical harmonics-space, this is called the power-spectrum C_l, and is defined by

$$C_l = \frac{1}{2l+1} \sum_{l=-l_{max}}^{lmax} a_{lm} a_{lm}^* \tag{2.47}$$

where the asterisk denote complex conjugation. That is, the power spectrum is the variance of the a_{lm}-coefficients. The power spectrum, calculated from current WMAP data is plotted in figure 2.6. As mentioned, beams will supress smaller scales, this effect is shown in figure 2.7. Another problem that will affect the power spectrum is *instrumental noise*. This is an uncertainty in the measurements due to instumental design. It will appear across the map as random fluctuations that are not correlated with the CMB or any foreground emission. This will affect the smaller scales, but with the opposite effect from beams. The power at large l's will be overestimated, as shown in figure 2.8.

CMB-maps are typically displayed using the Mollweide projection, an elliptical display with the equator being exatly twice the length of the meridian. The resolution is determined by the parameter N_{side}. The maps are first divided into

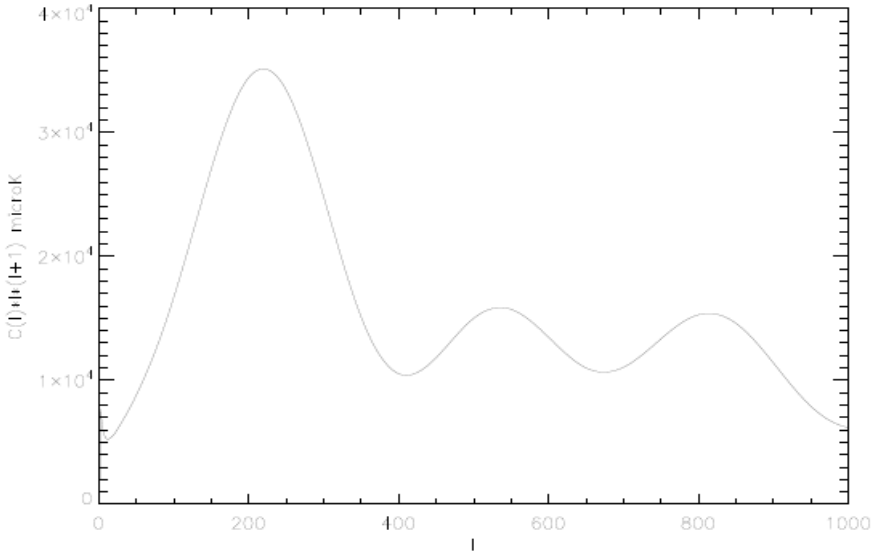

Figure 2.6: Power spectrum, without beam or noise

12 square pixels(See figure 2.9). These base-pixels can then also be divided into smaller parts, N_{side} gives the number of pixels that lie along one of the sides of the square. N_{pix}, the total number of pixels in a map is then given by

$$N_{pix} = 12N_{side}^2 \tag{2.48}$$

The Earth's atmosphere is almost opaque to the part of the electromagnetic spectrum in which we find the CMB. Therefore, measuring the CMB accurately requires detectors launched into space to observe from points above the atmosphere.

2.6.2 COBE

The COsmic Background Explorer (COBE) was a NASA mission launched in 1989, the first to offer high-precision measurements of the CMB. The satellite orbited Earth at an altitude of 900km, with an orbital period of 103 minutes [13]. It took 6 months to scan the entire sky.

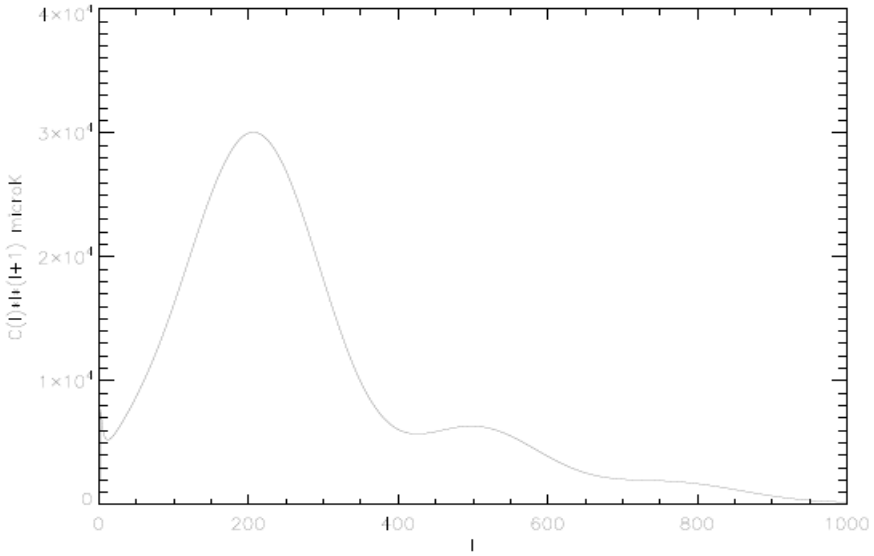

Figure 2.7: Power spectrum, with beam

The spacecraft had three instruments aboard, the Diffuse Infrared Background Experiment (DIRBE), the Differential Microwave Radiometer (DMR) and the Far Infrared Absolute Spectrophotometer (FIRAS). FIRAS was used to measure the absolute temperature of the CMB, found to be $2.725 \pm 0.002K$. DMR observed the anisotropies in the CMB, while DIRBE studied the Cosmic *Infrared* Background. Observations at frequencies above the microwave-part of the spectrum yields information about star-formation.

The DMR operated on three different frequencies, 31.5, 53, and 90 GHz. The sky was observed with a 7° FWHM beam. The resultant maps were drawn with 6144 pixels, and the power-spectrum was calculated with $l_{max} = 30$ [22].

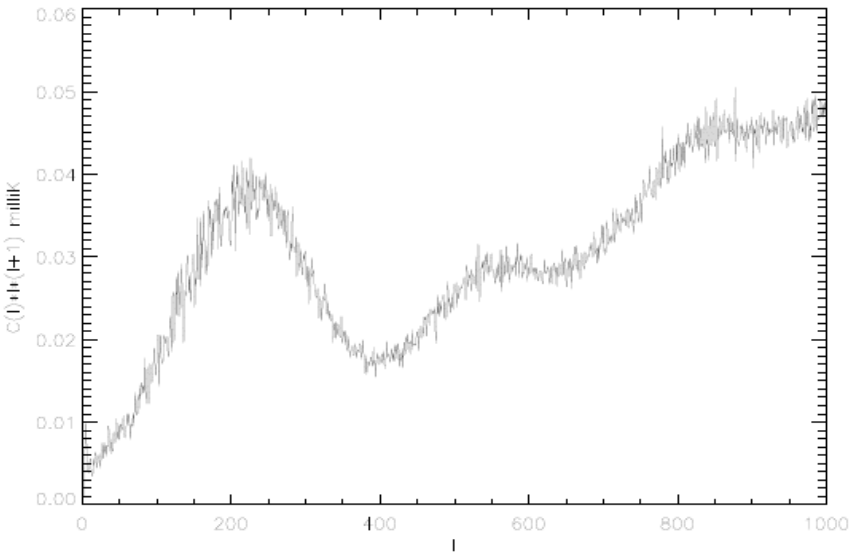

Figure 2.8: Power spectrum, with noise

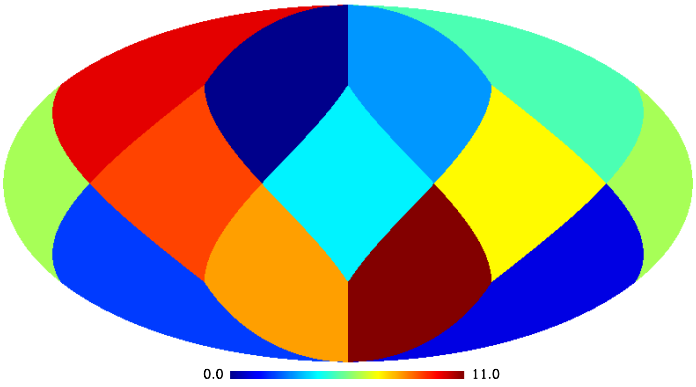

Figure 2.9: Mollweide projection, nside=1

2.6.3 WMAP

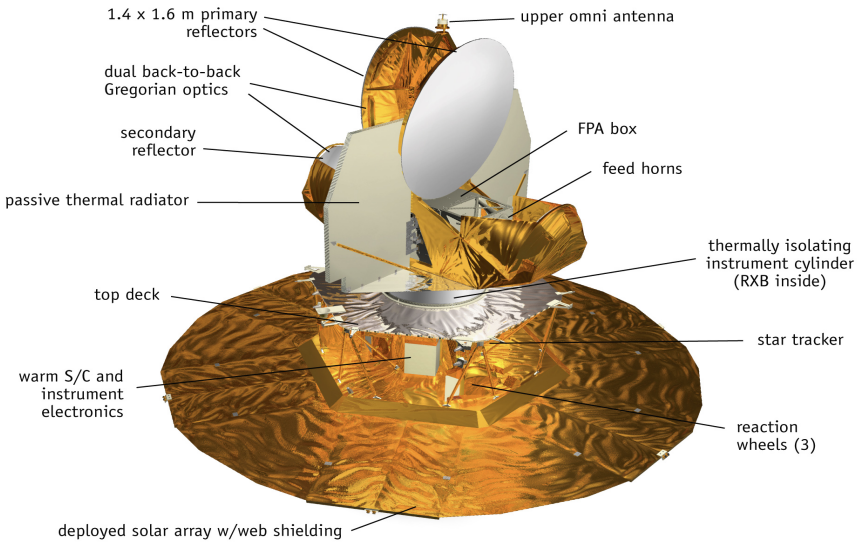

Figure 2.10: WMAP spacecraft

The Wilkinson Microwave Anisotropy Probe(WMAP) was launched June 30, 2001 from Cape Canaveral, Florida.
The probe orbits the L2 Lagrange point, about 1.5 million km from Earth. From this position, the telescope's view is not obstructed by the Sun, Earth or the moon. It covers about 30% of the sky every day, covering the full sky every six months [12]. The spacecraft is shown in figure 2.10 and the projects webpage can be found at http://map.gsfc.nasa.gov

The main feature of the spacecraft is the two back-to-back telescopes that measures the difference in temperature between two spots in the sky. The two points are separated by roughly 140°.
To provide more data to help with the removal of foreground contamination, WMAP uses five different frequency bands that are listed in table 2.1. The maps from the different bands are displayed in figure 2.6.3, showing the bands in order of increasing frequency.
The resolution of the the different bands are listed in column three of table 2.1. The five-year data allowed for an estimation of the power spectrum up to about $l_{max} = 1000$ [29].

$Band$	$Frequency(GHz)$	$Resolution(FWHM, degrees)$
K	22.8	0.93
Ka	33.0	0.68
Q	40.7	0.53
V	60.8	0.35
W	93.5	< 0.23

Table 2.1: WMAP frequencies

Figure 2.11: The five WMAP-bands

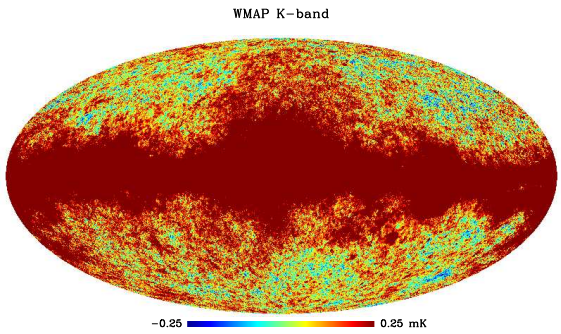

K-band

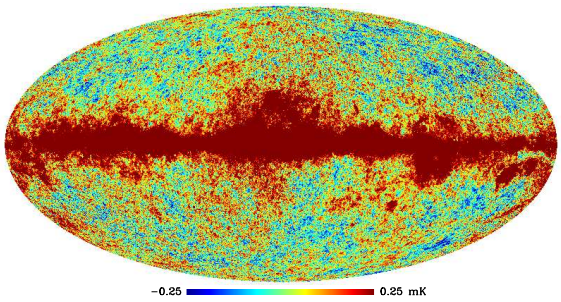

Ka-band

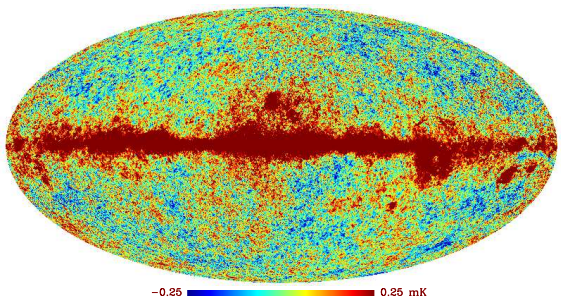

Q-band

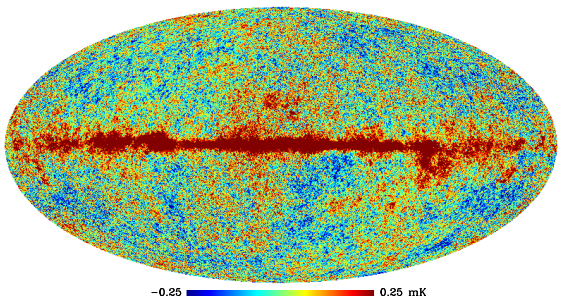

V-band

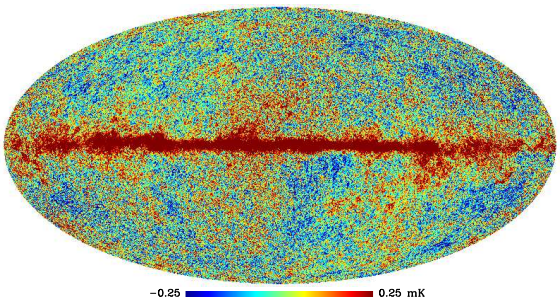

W-band

2.6.4 Planck

The Planck Surveyour will be launched in October, 2008. This ESA project aims to improve upon the results from WMAP by using nine frequency channels instead of WMAP's five. Divided between two different instruments, these channels will covers a frequency-range from 30GHz to about 850GHz, the 4 lowest frequencies being 30, 44, 70 and 100 GHz [11], comparable to those studied by WMAP(Table 2.1). The two instruments are called the Low Frequency and the High Frequency Instruments.
It will orbit the L2 Lagrange point, just like WMAP, and results will be released from 2010 onwards.
The frequencies covered and the associated beams are shown in table 2.2.

Frequency(GHz)	Resolution(FWHM,arcmins)
30	33
44	24
70	14
100	9.5
143	7.1
217	5.0
353	5.0
545	5.0
857	5.0

Table 2.2: Planck frequencies

The Planck results is expected to provide estimates of the power spectrum up to $l_{max} = 2000$.

2.6.5 Current results

The analysis of the data from WMAP, COBE and other CMB-experiments have yielded a much improved knowledge of the universe. In the context of this thesis, evidence of non-Gaussianity in the CMB is of most interest. Inflation-theory predicts a Gaussian distribution of the anisotropies, and evidence to the contrary would put the theory in serious jeopardy. Analysis of the WMAP-data gave three distinct anomalies, results that do not seem to agree with the theory of inflation.
First, there is a significant assymetry in the measured power between the northern

and southern hemisphere [24]. On large scales, the southern hemisphere shows much higher power than the north. One issue that should be taken into consideration here, is that the Sun is actually located roughly 20 parsecs above the galactic plane, meaning there should be more foreground sources in the southern directions [26]. However, several different and independent foreground removal methods applied separately to the two hemispheres, yields consistent results, which would seem to indicate the asymmetry can not be explained by foreground-residuals.

The second anomaly is the very low power found at the largest scales, particularly the quadru- and octopole. Both multipoles are found to have a low power, that is unlikely to a $1/20$ level [5]. The maps used to arrive at this conclusion, have had those parts of the sky most contaminated by foregrounds removed (See section 2.8 for details). It has been suggested that this cut causes the low power measured at the large scales, since much of that power may be located within the parts of the sky that is cut away [33]. The analysis done in [33] concludes that the low power, particularly of the quadrupole lies within reasonable limits, and is not really a cause for concern.

The third unusual discovery, and the one of most interest to this thesis, is the apparant lining up of the quadru- and octopole. [27] finds this alignment to be less than 0.01% likely in a Gaussian regime. Each multipole has a direction on the sky, in which it has the most power. This direction is found to be the same for $l = 2, 3$. A plot showing this alignment is displayed in figure 2.12.
In this thesis, we will investigate the influence of different foreground-removal methods on the measurement of this direction.

2.7 Physical processes behind foregrounds

The galactic emissions that lie in the microwave part of the electromagnetic spectrum is dominated by three different components, synchrotron , free-free and thermal dust emissions. There is evidence of a fourth component, [2] attributing it to synchtron radiation associated with star-forming regions. [35] suggests the emissions fit a spinning dust model.

Figure 2.13 shows how the three different contaminants vary with frequency, the WMAP bands are also marked in the plot. As the figure shows, the thermal dust component should vanish at low frequencies, and it was the discovery of an ap-

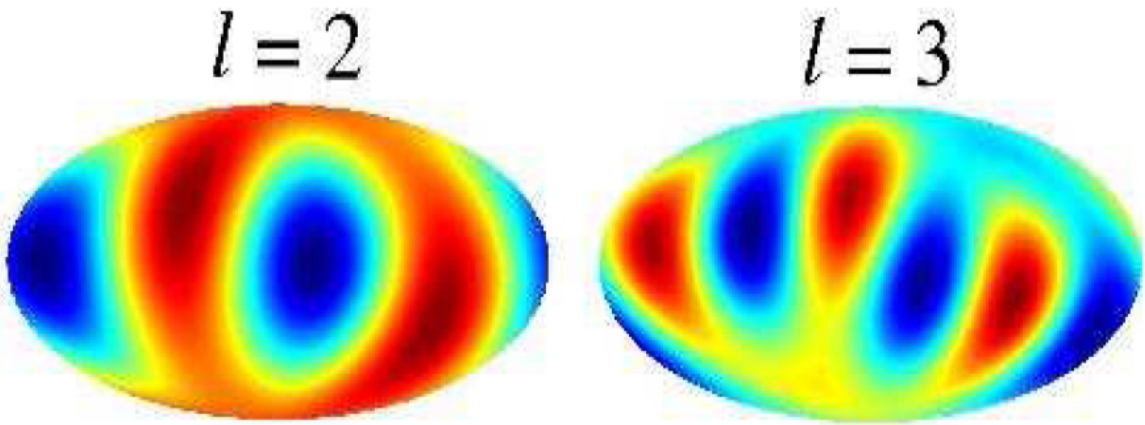

Figure 2.12: Multipole alignment, figure from [10]

parent dust-emission with an amplitude 500 times that expected from thermal dust emissions [7], between 20 and 40 GHz that has led to the postulating of a fourth component. The *spectral index* is a measure of how a given emission source radiates in relation to frequency. It is typically identified as

$$S = A\nu^{\beta} \tag{2.49}$$

where S is the flux, ν is frequency, A is the amplitude and β is the spectral index. All the methods applied in this thesis, assumes a constant spectral index for all foreground types across the entire sky. This is not a correct assumption, especially near the galactic plane there is large variations. Discovering the exact spectral indexes and how they vary is then of vital importance to creating accurate templates and models.

2.7.1 Synchrotron radiation

Synchrotron radiation is generated by ultra-relativistic particles accelerating through a magnetic field in a curved path. The primary galactic source of such radiation is

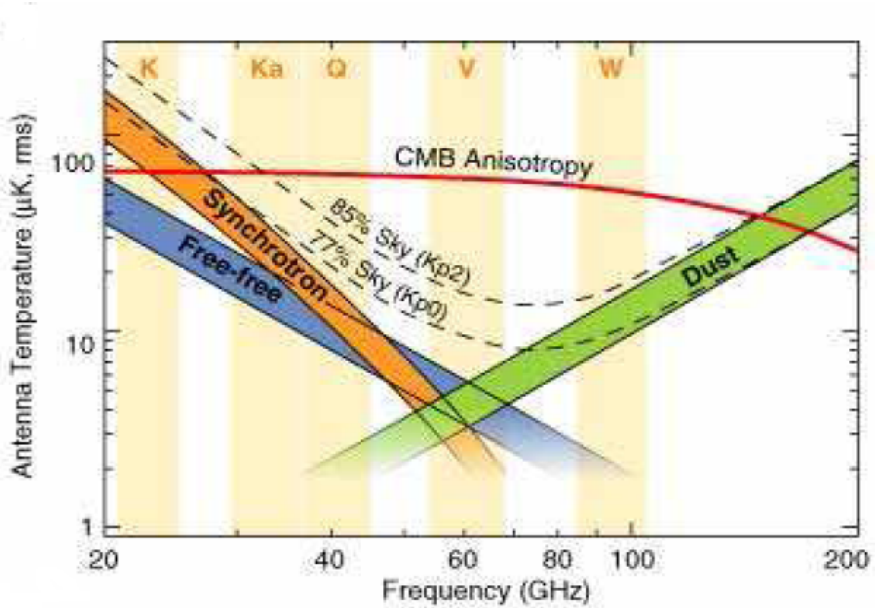

Figure 2.13: Galactic emission vs. frequency. From [2]

supernova remnants.
The radiated power P is

$$P = \frac{2Ke^2\gamma^4 v^4}{3c^3 r^2} \tag{2.50}$$

where e is the electron charge, v is the electrons velocity, r is the radius of it's path, c is the speed of light, K is Coulomb's constant and

$$\gamma = \frac{1}{\sqrt{1 - \frac{v^2}{c^2}}} \tag{2.51}$$

The energy spectrum of such radiation is characterized by the relativistic electron density. Since this density will vary greatly between regions of the galaxy, the spectral index will also change.
Between the radiating source and our instrument, there will be a number of intervening processes that causes the radiation to lose energy, such as Compton scattering and free-free collisions. Cosmic rays originating in the galactic halo will lose less energy from such interactions than those coming from within the plane of the galaxy itself, synchrotron radiation will therefore have a steeper spectral

index in areas near the galactic plane.
Observations of synchtrotron emission at low frequencies has yielded an approximate mean spectral index of $\beta \approx -2.7$. Observing another galaxy, which is orientated edge-on to our line of view, [8] found a spectral index ranging from -2.6 in the plane to -3.1 in the halo.

2.7.2 Thermal dust

Dust-particles that hold a higher temperature than the surrounding space will radiate heat in accordance with the first law of thermodynamics. This form of radiation exhibits an inverse relation between temperature and spectral index, meaning particles holding a higher temperature will have a lower flux. The dust grains in the galactic disc is assumed to have a typical temperature of 20K for the foreground templates used in [2], but this is a poor approximation [15]. The same article suggests the emissions recorded fits a model where there are two separate types of dust particles, silicate and carbon-dominated grains.
The average spectral index for thermal dust is $\beta = 2$. Different types of grains have different spectral indexe. Silicate grains are thought to dominate emissions at frequencies below 500 GHz. There is still reason to believe the spectral index will vary between different frequencies and regions in the sky due to different species of dust.
According to the model fitted in [15], the silicate grains have a spectral index $\beta = 1.7$, with a temperature of $\langle T \rangle = 9.5K$, the carbon-dominated grains $\beta = 2.7$, $\langle T \rangle = 16K$.

2.7.3 Free-free emission

Free-free emission, also called bremstrahlung, is produced by electrons scattering off ions. The term free-free refers to the electron not being captured by the ion in the process, both particles remain ”free” after the interaction. This type of radiation is typically produced in ionized Hydrogen clouds. The name bremstrahlung relates to the electron losing velocity in the interaction, ”brems” being German for ”brake”, whilst ”strahlung” means ”radiation”. The spectral index of free-free radiation is $\beta = -2.15$. Since this type of emission does not dominate the sky at any frequency, studies of the $H\alpha$-line is used as a substitute. Both free-free and $H\alpha$ are determined by the *emission measure* EM, defined as

$$EM = \int n_e^2 dl \tag{2.52}$$

where, n_e is the electron density and dl is a volume unit. Using this we can write the antenna temperature as

$$T_A = 1.44 EM_{cm^{-6}ps} \frac{[1 + 0.22\, ln(T_e/8000K) - 0.14\, ln(\nu/41GHZ)]}{(\nu/41GHz)^2 (t_e/8000K)^{1/2}} \tag{2.53}$$

where T_e is the electron temperature [2]. The spectral index is given by

$$\beta_{ff} = -2 - \frac{1}{10.48 + 1.5\, ln(T_e/8000K) - ln\nu_{GHz}} \tag{2.54}$$

T_e is unknown, but is assumed to be $T_e \approx 8000K$.

2.8 Foreground subtraction

While this thesis is concerned with the CMB, determining the exact nature of the galactic emissions themselves is also of interest. For the latter objective, the WMAP-team used the Maximum Entropy Method (MEM).
MEM seeks to separate the galactic emissions into the three different sources discussed in section 2.7. A complete skymap is modelled as

$$T_m(\nu, p) = S_{CMB}(\nu|p) T_{CMB}(p) + S_s(\nu|p) T_s(p) + S_{ff}(\nu|p) T_{ff}(p) + S_d(\nu|p) T_d(p) \tag{2.55}$$

where the subscripts denote the different contributions to the signal, CMB, synchrotron, free-free and thermal dust. p indicates pixel and ν is frequency. $S_x(\nu|p)$ is the spectrum of emission-type x, which takes into account the variation in spectral indices across the sky and $T_x(p)$ is the spatial distribution of x [2]. The latter is based on the templates that will be discussed further in section 2.8.1.
χ^2-minimization are used to to determine the best-fit spectral indices and spatial distributions. The results provide an assessment of how well the templates and corresponding coefficients used actually fits the data.

Since removing all signs of foreground contamination is beyond current algorithms, making the maps suitable for cosmological analysis requires some additional measures. Obviously, some parts of the sky are more contaminated than other, specifically in the plane of the galaxy. Simply observing the rest of the sky, and ignoring the parts most afflicted by unwanted radiation is done through the use of *masks*.
Masks are simply binary maps, with those pixels we wish to mask set equal to

zero, the rest equal to one. These maps are then superimposed on the skymaps to cancel out contribution from unwanted pixels.
The WMAP-team constructed their masks by removing pixels with an absolute value higher than some cutoff-point, shown in figure 2.14. To remove the fore-

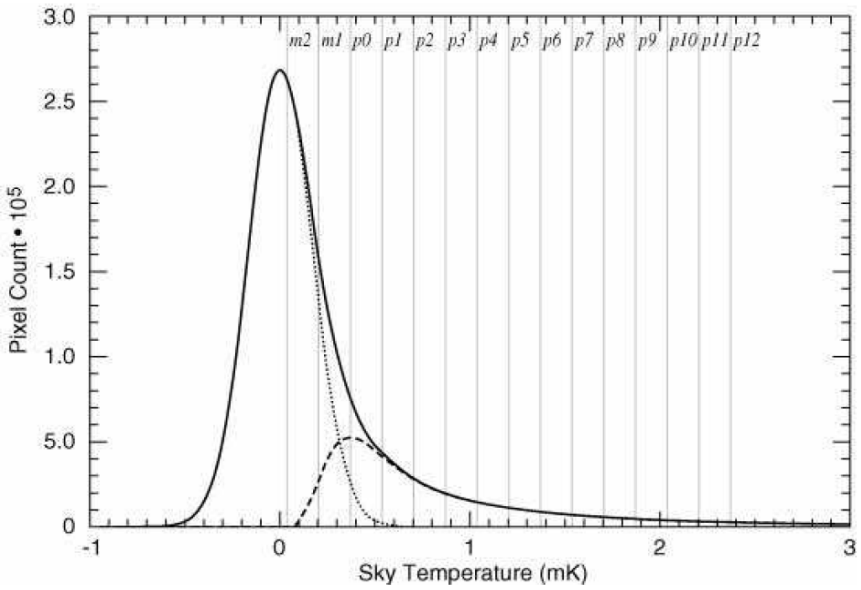

Figure 2.14: WMAP masks. From [2]

ground contamination from CMB-maps, this thesis will use three different approaches, External Template Fitting(ETF), Internal Linear Combination (ILC) and Wavelet based hIgh resolution Fitting of Internal Templates(WI-FIT).

2.8.1 External Template Fitting

Perhaps the simplest and most straight-forward of the methods applied in this paper, external template fitting(ETF) uses externally derived templates to clean the CMB-maps. While this approach may not provide much in terms of a deeper understanding of the physical nature of the foregrounds, it has the clear advantage of having well specified noise properties.
One external template is chosen to model each of the three different foreground

components discussed in section 2.1.5. These templates are drawn from other experiments in other frequency-ranges than those in which WMAP operates. A set of coefficients C^t are used with the templates to correct for the change in frequency, where t represents the three different types of foregrounds.
To model the synchrotron emission, we use the Haslam 408 MHz map [25]. The results from the WMAP teams implementation of the MEM, showed the resulting map not to be a great match at the WMAP frequencies, due to not taking into account that the spectral index varies across the sky [2]. This led to negative c^t, to avoid this problem only the Q-, V-, and W-bands will be examined. By appropriately scaling the templates, all c^t's will be positive. The coefficients are derived from the spectral indexes,

$$c^t(\nu) = A\nu^{\alpha} \tag{2.56}$$

K and A are constants to fit the templates to the WMAP-frequency range, ν is the frequency and α is the spectral index for t.
In the release of the three-year data, the Haslam map was replaced by an internal template, of the difference between the K and Ka-bands, just like in the WIFIT-method [3]. However, the Haslam-map is used in this thesis.

To represent free-free emission, the Finkbeiner $H\alpha$ map [14] is used. This is a composite of three different maps, the Virginia Tech Spectral Line Survey for the northern hemisphere, the Southern $H\alpha$ Sky Survey Atlas for the southern and The Wisconsin $H\alpha$ Mapper. $H\alpha$ is an emission line associated with the hydrogen atom, it is the first line in the *Balmer-series*. It lies within the visible region of the electromagnetic spectrum.
The thermal dust-template is from [15], which is again based on [32]. This map is based upon results from COBE and IRAS missions.
This set of templates will be referred to as the ***HFF***-set throughout this thesis.
We also used a second set of templates. In preparation of the Planck-mission, workgroups have been established that consider ways of separating the CMB from foreground emissions. This work has resulted in, among other things, a new set of templates that is considered better and more realistic than HFF. These new templates take into account changing spectral indexes, and they will therefore be a very useful test of the abilities of our applied methods to handle the spectral index-problem that we know the HFF-set does not provide. This new set of templates we will refer to as ***NFG***.

The full skymap T is written as

$$T = T_{CMB} + T_{dust} + T_{ff} + T_{sync} + n \tag{2.57}$$

that is a sum of a CMB-component and the three different foreground-types and the instrumental noise. Cleaning such a map is the done by assuming the galactic components can be described by the templates from above and the appropriate, frequency-dependent coefficients and subtracting them from the full map.

2.8.2 Internal Linear Combination

The second method we will use is the ILC. The idea is to form linear combinations of the different frequency maps, with constraints to minimize the foreground contamination while retaining the CMB-signal. A clear advantage in such an approach is that it does not rely on the use of external templates, instead using only the WMAP-data hence the name *internal*.
However, the WMA-team stressed that the resultant map was suitable only for visualisation purposes, and can not be relied on for precise CMB-analysis.
Writing a sky-map T as a sum of the CMB and foreground signals

$$T = T_{CMB} + T_{fg+n}(\nu) \tag{2.58}$$

where ν is frequency, of which the CMB is independent. T_{fg+n} is the combined signal from foregrounds and instrumental noise. We seek to suppress the foregrounds while retaining the CMB. The ILC-method suggests a map can also be written as

$$T = \sum_{i=1}^{5} w_i T(i) \tag{2.59}$$

where the sum is over the five WMAP-bands, and w_i is a set of weights. Inserting this into equation 2.58, we get

$$T = \sum_{i=1}^{5} w_i T_{CMB} + \sum_{i=1}^{5} w_i T_{fg}(i) \tag{2.60}$$

Since we wish to retain the CMB-signal,

$$\sum_{i=1}^{5} w_i = 1 \tag{2.61}$$

With the CMB begin independent of frequency, $\sum_{i=1}^{5} w_i T_{CMB} = T_{CMB}$. The trick is then to find the set of weights w that minimizes the foreground component of the signal, while still summing to one. This can done by searching for the minimum of the variance σ,

$$\sigma(T) = \sigma(T_{CMB}) + \sigma(\sum_{i=1}^{5} w_i T_{fg}(i)) \tag{2.62}$$

The WMAP-team did this using a non-linear method, without specifying the details [2]. In this thesis, we use the approach from [10]. This uses Lagrange multipliers (2.5) to find the weights, the details can be found in the algorithm-section.
Since the spectral indexes vary across the sky, the WMAP ilc-implementation divided the sky into 12 smaller regions, and calculated a set of weights for each. 11 of the regions lie within the Kp2-cut, see figure 2.14, and this approach yielded an asymmetry in the weights calculated. One particular region gave distinctly different weights from the other regions. This would seem to indicate a problem with the template-approach used with ETF, and is further evidence that assuming constant spectral indexes across the sky will corrupt results.

2.8.3 WI-FIT

The third foreground-cleaning method is called Wavelet based hIgh resolution Fitting of Internal Templates(WI-FIT). WI-FIT uses templates to clean the maps much like section 2.8.1, the difference being that these templates are not drawn from other frequencies than those we find the CMB at. Rather, they are created by taking the difference between two of the available WMAP-frequency bands. Since the CMB-component is independent of frequency, it will cancel out, leaving only the difference in foreground contributions and a noise component.
Each frequency-band is then cleaned by subtracting a linear combination of internal templates. The number of internal templates must be equal to the number of foreground emission-types, which is three in our case (Thermal dust, free-free and synchrotron). Thus, if we write a complete skymap as

$$T_\nu = T_{CMB} + n_\nu + \sum_{f=1}^{N_f} c_\nu^f F^f \tag{2.63}$$

where the sum is over the number of foreground-components f, and F^f is the foreground-contribution from type f. c_ν^f are coefficients that determine the strength of component f at frequency ν. n is the instumental noise.
To simulate the F^f-components, WI-FIT uses templates defined as

$$D^{\nu\nu'} = T_\nu - T_{\nu'} \tag{2.64}$$

Using these new templates, we can rewrite the full skymap as

$$T_\nu = T_{CMB} + n_\nu + \sum_{t=1}^{N_t} \tilde{c}_\nu^t (D^t - \delta n^t) \tag{2.65}$$

where the sum now goes over templates t. As specified above, $N_f = N_t$.
Since the internal templates will contain noise-contributions from the two different frequency-maps involved in their creation, there is an extra element $\delta n = n_\nu - n_{\nu'}$ introduced in the sum.
Calculating the $\tilde{c}_\nu^t$ is done by a χ^2-minimization, however doing this in pixelspace is not possible for higher resolutions, as such an approach requires inverting a correlation-matrix of size $N_{pix} \times N_{pix}$. Therefore, WI-FIT uses wavelet-transforms to do the calculation in wavelet-space where pixel-pixel correlations are smaller. Thus, the size of the correlation-matrix will be determined only by scale-scale-correlations. [23] used 13 scales, which gives a correlation-matrix of size 13×13 to invert, as opposed to one of $3mill \times 3mill$ in pixel-space assuming an $N_{side} = 512$.

The noise in the internal templates leads to a bias in the calculation of the coefficients $\tilde{c}_\nu^t$. [23] details a bias-correction approach to work around this problem. However, since noise mostly affects the smaller wavelet scales, we can convolve the maps with a large beam to suppress the smaller scales and thus minimize the influence of the noise on the final results.

As mentioned in section 2.8.2, the sky can be divided into smaller sections to get more accurate estimates of the spectral index in various localizations on the sky. In this thesis, we worked only with complete skymaps, so the WI-FIT method implementation assumed a constant spectral index over the complete sky.

Chapter 3

Algorithm

The implementation of the cleaning algorithms makes use of the Healpix-package([20]), a library of visualization and computational software suitable to process and manage the large amount of data from present day CMB-experiments [21].
The goal of this section is to make use of the three different methods of foreground-removal detailed in section 2.8, and to derive results suitable for comparison between the three so as to be able to determine the reliability, accuracy and effectiveness of the individual approaches.
To achieve this, Monte Carlo simulations of the CMB map will be generated and then cleaned. The direction of the quadru- and octo-poles will be determined for each individual simulation in three instances, the original simulated map, the map with a foreground model added and for the cleaned map. Comparison between the cleaned and simulated versions will then provide a measure of the algorithm's effectiveness.
Apart from a visual inspection of the resulting maps, the cleaning processes performance will be assessed by measuring the difference in direction of the quad- and octopoles between the simulated and cleaned maps.
A temperature map of CMB-observations can be written as,

$$T_i^\nu = T_i^{CMB} + n_i^\nu + \sum_{t=1}^{N_t} C_t^\nu s_i^t \tag{3.1}$$

where T is the temperature in pixel i for frequency-band ν. The sum is over the total number of galactic foreground-components N_t, with s_i^t being the temperature from component t in pixel i. n_i^ν is the instrumental noise. C_t^ν is a set of coefficients

to fit the templates to the appropriate frequency bands, the values that were used with the templates described in section 2.8.1 are given in table 3.1.

For all three methods, the aim is to separate the CMB-component and suppress the rest.

3.1 Calculation of preferred axis

As mentioned in section 2.6.5, there is an issue with the directions of the quadru- and octopole lining up in the WMAP-data. Were we to plot maps containing only one of these poles, it would appear as a few, large spots scattered around the sky. In the WMAP-data, not only do all these spots appear to line up along a common axis. In addition, this axis appears to be the same for both the quadru- and octopole. In our approach, we will calculate the direction of this axis in our simulated maps at different stages in the algorithm to investigate the impact of foregrounds and the foreground-removal methods on the direction of those two multipoles.

Defining the axis $\hat{\mathbf{n}}$, we can write the spherical harmonics transform of an anisotropy skymap as a wave function

$$T(\hat{\mathbf{n}}) = \varphi(\hat{\mathbf{n}}) \tag{3.2}$$

To find the direction, we find the axis around which

$$\left\langle \varphi \left| (\hat{\mathbf{n}} \cdot \mathbf{L})^2 \right| \varphi \right\rangle = \sum_m m^2 \left| a_{lm}(\hat{\mathbf{n}}) \right|^2 \tag{3.3}$$

is maximized [10]. The actual implementation was done using computer-code written by my supervisor Frode K. Hansen.

3.2 ETF

As described in section 2.8.1, External Template Fitting is probably the simplest way of cleaning datamaps. Models of the foreground contamination are created by using data from other experiments. These templates are then fitted to the WMAP frequency channels by a set of coefficients. The templates used are described in section 2.8.1.

The approach taken here aims to clean the Q, V and W-bands of galactic foreground contamination. These bands contain less galactic emissions than the K

and Ka-bands(See figure 2.13), and results can be expected to be better for the former three bands.
500 Monte Carlo simulations for each channel are created and the direction of the quadrupole and octopole are calculated. The Haslam and Finkbeiner foreground templates, multiplied by the coefficients given in table 3.1, are then added, and the directions of the 2 multipoles are found again. Finally, a χ^2-minimization is used to attempt to recover the coefficients from table 3.1 for each simulation. The templates, this time multiplied with the recovered coefficients are then subtracted from the map, and the directions are computed one last time.

The maps are created with $Nside = 512$, the same as the original WMAP-maps. $lmax$ is set to 1000. A set of a_{lm}-coefficients are created, drawn from a distribution defined by the power spectrum calculated from the WMAP-data [17]. In order to make the simulations resemble the WMAP data, the simulated maps are smoothed with the band-specific beams defined by the WMAP instrument with the resolution given in table 2.1. A reverse spherical harmonics-transform(Section 2.2) produces the map, before the noise associated with each channel is added.
The actual code for the first part, the creation CMB-maps, the smoothing with the appropriate beams from WMAP and the adding of noise is sketched in listing 3.1. Note the loops over bands and simulations(sims), these continue through the entire code, meaning each map is put through all steps of the process before the process moves on to the next simulation.
The noise is randomized by multiplying the standard deviation given by the WMAP-specifications for the appropriate pixel and band, with a random number created outside the code shown.
The function $align$ calculates the array mom, which is the sum over m given in equation 3.3, which is then passed to $finddir$ to determine the direction of the quadru- and octopole. These directions are returned in polar coordinates θ and ϕ, in a system where the center of the galaxy is defined as the origin ($\theta = \phi = 0$).

$Band$	Dust	FreeFree	Synchrotron
K	7.00	10.20	28.0
Ka	2.70	4.70	7.50
Q	1.59	2.24	2.78
V	1.00	1.00	1.00
W	1.60	0.45	0.35

Table 3.1: ETF coefficients

Listing 3.1: Creation of CMB-maps

```
do band=0, 2  {
  do sim=0, nsims-1 {
  !!Create a new set of spherical harmonics-
  !!coefficients, drawn from powerspectrum 'cl',
  !!and put them in array alm
    call create_alm(nside, lmax, cl, alm)

!!Smooth with WMAP-beams
  alm=alm*beam(band)

!!Transform from frequency domain
!!to pixelspace
  call alm2map(nside,lmax,alm,map)

!!Finally, noise is added
  do j=0, npix-1 {
    noise_coef=noise(band,j)*rnd_nmbr
    map(j)=map(j)+noise_coef
  }
 !!Calculate direction of quadrupole
 !!and octopole
 CALL align(npix, map, mom)
 CALL finddir(nside, npix, mom, theta, phi)
```

Listing 3.2 shows the next step, adding the foreground templates. The actual reading of the files, and multiplication with the band-specific coefficients(See table 3.1 are done outside the main pipeline, but is included here for completeness. The directions of the two multipoles of interest are found in the same way as above.

Listing 3.2: Adding foregrounds

```
 !!Read Haslam and Finkbeiner templates
open(12,file=dust_template.unf)
read(12) fore_dust(0,:)
close(12)
open(12,file=freefree_template.unf)
read(12) fore_ff(0,:)
close(12)
open(12,file=synchrotron_template.unf)
read(12) fore_syn(0,:)
close(12)

!!Create foregrounds for the 3 bands
!! 0=Vband, 1=Wband, 2=Qband
   fore_ff(0,:) =fore_ff(0,:)*ff_vband_coef
   fore_dust(0,:)=fore_dust(0,:)*dust_vband_coef
   fore_syn(0,:)=fore_syn(0,:)*syn_vband_coef
   fore_ff(1,:) =fore_ff(0,:)*ff_wband_coef
   fore_dust(1,:)=fore_dust(0,:)*dust_wband_coef
   fore_syn(1,:)=fore_syn(0,:)*syn_wband_coef
   fore_ff(2,:)=fore_ff(0,:)*ff_qband_coef
   fore_dust(2,:)=fore_dust(0,:)*dust_qband_coef
   fore_syn(2,:)=fore_syn(0,:)*syn_qband_coef


 !!! Continuing the main algorithm:


 !!Add the foreground-templates
    do j=0, npix-1 {
      fullmap(band, j)=map(band,j)+fore_dust(band,j)
                    +fore_ff(band,j)+fore_syn(band,j)
    }

 !!Calculate direction of quadrupole and octopole
   CALL align(npix, fullmap, mom)
   CALL finddir(nside, npix, mom, theta, phi)
```

The cleaning process aims to recover the coefficients in table 3.1. To accomplish this, we seek to minimize what is known as the χ^2-distribution. This has the general form

$$\chi^2 = \sum_i \frac{(x_i - \mu)^2}{\sigma^2} \tag{3.4}$$

If the value x_i deviates significantly from the expected value μ, a large value of χ^2 will result. Specifying the above equation to our case

$$\chi^2 = \sum_i \frac{(T_i - (\sum_f C^f F_i^f))^2}{\sigma_i^2} \tag{3.5}$$

where i indicates pixels in a map, f is type of foreground emission(dust, freefree or synchrotron), T is the temperature map and F is the foreground templates. C is then the coefficients we wish to find. σ_i is the variance for pixel i. A pixel with a large variance will then be given less weight than one with a small variance. This is actually an approximation, the true χ^2 value is given by

$$\chi^2 = \sum_i (T_i - \sum_f C^f F_i^f) C_{ij}^{-1} \sum_j (T_j - \sum_f C^f F_j^f) \tag{3.6}$$

where C_{ij} is the correlation-matrix between pixels i and j. However, inverting such a matrix would be too time-consuming, so we instead make the assumption there are no pixel-to-pixel correlations, and design a correlation-matrix that is diagonal, with the diagonal elements equal to σ_i, and all other elements being set equal to zero. Inverting a diagonal matrix yields another diagonal matrix with the diagonal elements $C_{ii}^{-1} = 1/C_{ii}$, in our case $1/\sigma^2$. This gives us equation 3.5, which we can minimize to find the coefficients that best fit the data.
Expanding eq. 3.5, we get

$$\chi^2 = \sum_i \frac{(T_i - C^0 F_i^0 - C^1 F_i^1 - C^2 F_i^2)^2}{\sigma_i^2} \tag{3.7}$$

Minimizing the χ^2-statistic is done by differentiating this equation, and setting the result equal to zero. The differentiation is done with regards to the coefficients C. The calculation shown is only for C^0, but it can easily be extended to solve for the other two coefficients.

$$\frac{\partial \chi^2}{\partial C^0} = \sum_i \frac{2(T_i - C^0 F_i^0 - C^1 F_i^1 - C^2 F_i^2)(-F_i^0)\sigma_i^2}{\sigma_i^4} \tag{3.8}$$

Isolating the C^0-term:

$$\frac{\partial \chi^2}{\partial C^0} = \sum_i 2\frac{(T_i - C^1 F_i^1 - C^2 F_i^2)(-F_i^0)}{\sigma_i^2} + \sum_i 2\frac{C^0 F_i^0 F_i^0}{\sigma_i^2} \tag{3.9}$$

Setting the derivate equal to zero and cleaning up:

$$\sum_i \frac{C^0 F_i^0 F_i^0}{\sigma_i^2} = \sum_i \frac{(T_i - C^1 F_i^1 - C^2 F_i^2)(F_i^0)}{\sigma_i^2} \tag{3.10}$$

Finally, we solve for C^0:

$$C^0 = \frac{\sum_i \frac{(T_i - C^1 F_i^1 - C^2 F_i^2)(F_i^0)}{\sigma_i^2}}{\sum_i \frac{F_i^0 F_i^0}{\sigma_i^2}} \tag{3.11}$$

The solutions for C^1 and C^2 can be shown to be:

$$C^1 = \frac{\sum_i \frac{(T_i - C^0 F_i^0 - C^2 F_i^2)(F_i^1)}{\sigma_i^2}}{\sum_i \frac{F_i^1 F_i^1}{\sigma_i^2}} \tag{3.12}$$

$$C^2 = \frac{\sum_i \frac{(T_i - C^0 F_i^0 - C^1 F_i^1)(F_i^2)}{\sigma_i^2}}{\sum_i \frac{F_i^2 F_i^2}{\sigma_i^2}} \tag{3.13}$$

Moving all terms containing C-coefficients to the left side produces three equations:

$$C^0 \sum_i \frac{F_i^0 F_i^0}{\sigma_i^2} + C^1 \sum \frac{F_i^1 F_i^0}{\sigma_i^2} + C^2 \sum \frac{F_i^2 F_i^0}{\sigma_i^2} = \sum_i \frac{T_i F_i^0}{\sigma_i^2} \tag{3.14}$$

$$C^0 \sum \frac{F_i^0 F_i^1}{\sigma_i^2} + C^1 \sum_i \frac{F_i^1 F_i^1}{\sigma_i^2} + C^2 \sum \frac{F_i^2 F_i^1}{\sigma_i^2} = \sum_i \frac{T_i F_i^1}{\sigma_i^2} \tag{3.15}$$

$$C^0 \sum \frac{F_i^0 F_i^2}{\sigma_i^2} + C^1 \sum \frac{F_i^1 F_i^2}{\sigma_i^2} + C^2 \sum_i \frac{F_i^2 F_i^2}{\sigma_i^2} = \sum_i \frac{T_i F_i^2}{\sigma_i^2} \tag{3.16}$$

which can be solved as a standard matrix-equation,

$$A\vec{x} = \vec{b} \tag{3.17}$$

with the matrix A given by:

$$\begin{pmatrix} \sum_i \frac{F_i^0 F_i^0}{\sigma_i^2} & \sum \frac{F_i^1 F_i^0}{\sigma_i^2} & \sum \frac{F_i^2 F_i^0}{\sigma_i^2} \\ \sum \frac{F_i^0 F_i^1}{\sigma_i^2} & \sum_i \frac{F_i^1 F_i^1}{\sigma_i^2} & \sum \frac{F_i^2 F_i^1}{\sigma_i^2} \\ \sum \frac{F_i^0 F_i^2}{\sigma_i^2} & \sum \frac{F_i^1 F_i^2}{\sigma_i^2} & \sum_i \frac{F_i^2 F_i^2}{\sigma_i^2} \end{pmatrix}$$

The vectors $\vec{x}$:

$$\begin{pmatrix} C^0 \\ C^1 \\ C^2 \end{pmatrix}$$

and $\vec{b}$:

$$\begin{pmatrix} \sum_i \frac{T_i F_i^0}{\sigma_i^2} \\ \sum_i \frac{T_i F_i^1}{\sigma_i^2} \\ \sum_i \frac{T_i F_i^2}{\sigma_i^2} \end{pmatrix}$$

Solving this system is then done by inverting A and solving for $\vec{(x)}$,

$$\vec{x} = A^{-1}\vec{b} \tag{3.18}$$

The implementation of this process is outlined in listing 3.3.
σ^2 is composed of two parts, the variance in the noise and in the CMB. A randomly simulated CMB-map is used to find the variance(σ_s) in the CMB, through

$$\sigma_s = \frac{1}{N_{pix}} \sum_{i=0}^{N_{pix}} p_i^2 \tag{3.19}$$

where p_i is the pixel.
The noise-variance(σ_n) is determined by the specifications of the WMAP-instrument, squaring the standard deviation. σ is the sum of these two components. Then the matrix A is constructed, for containing the foreground templates.

Listing 3.3: Cleaning with ETF

```
!!First calculate the variance sigma,
!!using a randomly created CMB-map
do j=0, npix-1 {
   temp=some_map(j)^2
   sigma_s=sigma_s+temp
}
 sigma_s=sigma_s/npix

   do j=0, npix-1 {
       sigma_n(band, j) = stddev(band, j)^2
       sigma(band, j)=sigma_s+sigma_n(band,j)
   }

!!Calculate matrix
   do j=0, npix-1 {
       A(band,0,0)=A(band,0,0)+(for(0,j)*for(0,j)/sigma(band,j))
       A(band,1,0)=A(band,1,0)+(for(1,j)*for(0,j)/sigma(band,j))
       A(band,2,0)=A(band,2,0)+(for(2,j)*for(0,j)/sigma(band,j))
       A(band,1,1)=A(band,1,1)+(for(1,j)*for(1,j)/sigma(band,j))
       A(band,2,1)=A(band,2,1)+(for(2,j)*for(1,j)/sigma(band,j))
       A(band,2,2)=A(band,2,2)+(for(2,j)*for(2,j)/sigma(band,j))
 }
!!Since this is a symmetric matrix, we can reverse the indexes
   A(band,0,1)=A(band,1,0)
   A(band,0,2)=A(band,2,0)
   A(band,1,2)=A(band,2,1)

!Construct right side of the matrix equation,
!the vector b
   do j=0, npix-1 {
       b(band,0)=b(band,0)+fullmap(band,j)*for(0,j)/sigma(band,j)
       b(band,1)=b(band,1)+fullmap(band,j)*for(1,j)/sigma(band,j)
       b(band,2)=b(band,2)+fullmap(band,j)*for(2,j)/sigma(band,j)
   }

!!!! To solve the system, invert A
   CALL inverse(A(band,:,:))

!!! Finally, solve for the coefficient vector x
   x(band,:,i)=matmul(b(band,:),A(band,:,:))
```

The algorithm ends with using the calculated coefficients to clean the maps, subtracting the foreground templates multiplied by the appropriate coefficients. This is shown in listing 3.4

Listing 3.4: Final cleaning of maps

```
!!!Create new foreground-maps
!!! 0=dust, 1=freefree, 2=synchrotron
  do j=0, npix-1 {
     simfg_dust(j)=for(0,j)*x(band,0,i)
     simfg_ff(j)=for(1,j)*x(band,1,i)
     simfg_syn(j)=for(2,j)*x(band,2,i)
  }

!!!Clean the maps with the new foreground maps
  do j=0, npix-1 {
     new_map(j)=fullmap(band,j)-simfg_dust(j)
                -simfg_ff(j)-simfg_syn(j)

  }
 !!Calculate direction of multipoles in the new maps
 CALL align(npix, new_map, mom)
 CALL finddir(nside, npix, mom, theta, phi)


   } !!End loop over simulations i
 } !!End loop over band
```

3.3 ILC

The Internal Linear Combination (ILC) method was first presented with the release of the WMAP first-year data [2]. By using proper constraints, foreground signals can be suppressed while retaining the CMB. A clear advantage to such an approach is that its results are not reliant on external templates, or any prior knowledge of the galactic foreground signals.

A complete skymap may be written as

$$T = T_{CMB} + T_{other} \tag{3.20}$$

that is, as a sum of the CMB and other sources, such as foregrounds and noise. We wish to suppress the residuals while keeping the CMB-signal intact. T_{CMB} is obviously independent from both T_{other} and of frequency. T_{other} on the other hand, will change according to frequency. For k different frequency maps, each WMAP-band can then be written as

$$T_k = T_{CMB} + T_{other}(k) \tag{3.21}$$

Forming the linear combination

$$T = \sum_{i=1}^{k} w_i T(i) \tag{3.22}$$

with the constraint

$$\sum_{i=1}^{k} w_i = 1 \tag{3.23}$$

we can write the final map as

$$T = T_{CMB} + \sum_{i=1}^{k} w_i T_{other}(i) \tag{3.24}$$

This guarantees the response to the CMB-signal will always be unity, and we are free to choose the weights w that limits the residual component to it's minimum. To compute the weights, we will use Lagrange multipliers(2.5).

As with the ETF, we create 500 CMB-simulations, apply foreground templates and then clean the maps using the ILC-algorithm. However, unlike the ETF-algorithm we will not clean each band separately, but instead use all 5 maps from the different frequencies to create one final, cleaned map. For this, the different maps need to be convolved with a common resolution, using a Gaussian beam of $1\,\mathrm{deg}$ FWHM, the same as used in both [2] and [10].
Again, we use $N_{side} = 512$.
The creation of the CMB-maps is pretty much the same as in listing 3.1, with the only difference being that each realization is copied five times so we have

5 different maps to represent the five WMAP bands. The foreground templates are then added. As with the ETF, both the Finkbeiner and Haslam templates are used, together with the coefficients in table 3.1 and the Planck workgroup templates in separate processes. The maps, now complete with both CMB, noise and foregrounds then have the band-specific WMAP-beams removed, and they are all convolved with the common, larger beam.
As mentioned, Lagrange multipliers (2.5) are used to find the weights. We seek then to minimize the variance of a sum over 5 frequency maps, constrained by the sum of the weights being equal to one. This guarantees we retain the CMB, whilst the frequency-dependent foregrounds and noise are suppressed. The variance of map T from equation 3.22 is given by

$$\sigma^2(T) = \langle T^2 \rangle - \langle T \rangle^2 \tag{3.25}$$

$$= \frac{1}{N_{pix}} \sum_{p=1}^{N_{pix}} \left[\sum_{i=1}^{5} w_i T_i(p) \right]^2 - \left(\frac{1}{N_{pix}} \sum_{p=1}^{Npix} \left[\sum_{i=1}^{5} w_i T_i(p) \right] \right)^2 \tag{3.26}$$

$$= \sum_{i=1}^{5} \sum_{j=1}^{5} w_i w_j \left(\frac{1}{N_{pix}} \sum_{p=1}^{N_{pix}} T_i(p) T_j(p) - \left[\frac{1}{N_{pix}} \sum_{p=1}^{N_{pix}} T_i(p) \right]^2 \right) \tag{3.27}$$

$$= \vec{w}^T \mathbf{C} \vec{w} \tag{3.28}$$

where w is the weights, and $\mathbf{C}$ is the covariance matrix defined as

$$C_{ij} = \langle \Delta T_i \Delta T_j \rangle = \frac{1}{N_{pix}} \sum_{p=1}^{N_{pix}} \left[T_i(p) - \langle T_i \rangle \right] \left[T_j(p) - \langle T_j \rangle \right] \tag{3.29}$$

Our task is then to minimize the function

$$f(\vec{w}) = \sum_{i,j=1}^{5} w_i C_{ij} w_j \tag{3.30}$$

with the constraint

$$g(\vec{w}) = \sum_{i=1}^{5} w_i = 1 \tag{3.31}$$

Using Lagrange multipliers, we then look for the points along $g(\vec{w})$ that satisfies

$$\nabla f(\vec{w_0}) = \lambda \nabla g(\vec{w_0}) \tag{3.32}$$

The partial derivates of the two functions in equations 3.30 and 3.31 are

$$\frac{\partial f}{w_i} = 2\sum_{j=1}^{5} C_{ij} w_j \tag{3.33}$$

and

$$\frac{\partial g}{w_i} = 1 \tag{3.34}$$

We can now construct 6 equations with 6 unknowns, which is solved as a matrix equation, $A\vec{x} = \vec{b}$. The first five equations are

$$2\sum_{j=1}^{5} C_{ij} w_j - \lambda = 0 \tag{3.35}$$

for each of the five values of i, and the sixth equation is just equation 3.31. Constructing the matrix A,

$$\begin{pmatrix} 2\mathbf{C}_{0j} & -1 \\ 2\mathbf{C}_{1j} & -1 \\ 2\mathbf{C}_{2j} & -1 \\ 2\mathbf{C}_{3j} & -1 \\ 2\mathbf{C}_{4j} & -1 \\ \vec{1}^T & 0 \end{pmatrix}$$

the vectors $\vec{x}$

$$\begin{pmatrix} w_0 \\ w_1 \\ w_2 \\ w_3 \\ w_4 \\ \lambda \end{pmatrix}$$

and $\vec{b}$

$$\begin{pmatrix} 0 \\ 0 \\ 0 \\ 0 \\ 0 \\ 1 \end{pmatrix}$$

Inverting A, and solving for $\vec{x}$ then gives us our weights. The coding to perform

this operation is shown in listing 3.5.
First, the average pixelvalues are found, and then used to calculate the covariance matrix. This matrix is also padded with -1's, 1's and a 0 to complete the set of equations to be solved. The weights are then found by inverting this matrix, and the cleaned map is created.

Listing 3.5: Cleaning with ILC

```
 !!Find the average pixelvalue
  avemaps(:)=0.d0
  do g=0, band-1
     avemaps(g)=avemaps(g)+fullmaps(g,:)/npix
   end do

!!Create covariance matrix
  covar(:,:)=0.d0
    do a=0, band-1
     do b=0, band-1
        covar(a,b)=2*(covar(a,b)+((fullmaps(a,:)
                   -avemaps(a))*(fullmaps(b,:)
                   -avemaps(b))))
        covar(5,b)=-1.d0
     end do
      covar(a,5)=1.d0
    end do
   covar(5,5)=0.d0
   covar(:,:)=covar(:,:)/npix

!!Invert covariance matrix
  CALL invert(covar,invcovar)

!!Create the vector b
  b(0:4)=0.d0
  b(5)=1.d0
!!Calculate the vector containing the weights
  weights(:)=b*invcov
 !!Create the final, cleaned map using
 !!the weights
   cleanmaps(:)=weights(0)*fullmaps(0,:)
                +weights(1)*fullmaps(1,:)
                +weights(2)*fullmaps(2,:)
                +weights(3)*fullmaps(3,:)
                +weights(4)*fullmaps(4,:)
```

3.4 WI-FIT

The WI-FIT algorithm uses a linear combination of internal templates to clean the skymaps. As with ETF, we wish to clean the Q-,V- and W-bands.
A full skymap is written as

$$T_i^\nu = T_i^{CMB} + n_i^\nu + \sum_{f=1}^{N_f} c_f^\nu F_i^f \tag{3.36}$$

where ν is frequency, n is noise, f is foreground type and F is the foreground component for pixel i. We wish to create a model of the galactic emissions ($\sum_{f=1}^{N_f} c_\nu^f F_i^f$), by using internal templates defined by

$$D_i^{\nu\nu'} = T_i^\nu - T_i^{\nu'} = \sum_{f=1}^{N_f} (c_f^\nu - c_f^{\nu'}) F_i^f + \delta n_i^{\nu\nu'} \tag{3.37}$$

Inserting this into equation 3.36, results in

$$T_i^\nu = T_i^{CMB} + n_i^\nu \sum_{t=1}^{N_t} \tilde{c}_t^\nu (D_i^t - \delta n^t) \tag{3.38}$$

where $t = \nu\nu'$, and $N_f = N_t$ since we need the same amount of templates as we have foreground components. Unfortunately, δn^t is an unknown noise contribution. We will assume it is equal to zero, but this will introduce a bias in results. Since noise is mostly dominant on small scales, we implement a large beam to suppress those scales, thus hoping to reduce the bias.
Solving equation 3.38 in pixel-space is not possible for high resolutions (See section 2.8.3), so we use wavelet transforms instead. (Section 2.4). Pixel-pixel correlations can be ignored in wavelet-space, so we only have to consider scale-scale correlations.
Two cross-correlation coefficients are defined,

$$X_S^{\nu t} = \sum_i w_{iS}^\nu w_{iS}^t \tag{3.39}$$

and

$$X_S^{tt'} = \sum_i w_{iS}^t w_{iS}^{t'} \tag{3.40}$$

where $w_{i_s}^{\nu}$ is the wavelet transform of T_i^{ν} for scale S, and w_{iS}^{t} is the transform of internal template D_i^t. The transforms are done using the Spherical Mexican Hat wavelets, using 13 different scales.
We can now define the χ^2 to minimize as

$$\chi^2 = \sum_{\nu T} \sum_{SS'} (X_S^{\nu T} - \sum_t \tilde{c}_t^{\nu} X_S^{tT}) C_{SS'}^{-1} (X_{S'}^{\nu T} - \sum_t \tilde{c}_t^{\nu} X_S^{\prime tT}) \tag{3.41}$$

Finding the coefficients $\tilde{c}_t^{\nu}$ is done in much the same way as in the ETF-algorithm, through solving a matrix-equation

$$\sum_t \tilde{c}_t^{\nu} M_{tf} = B_f^{\nu} \tag{3.42}$$

where

$$M_{tf} = \sum_{t'} \sum_{SS'} X_S^{ft'} C_{SS'}^{-1} X_{S'}^{tt'} \tag{3.43}$$

and

$$B_f^{\nu} = \sum_{t'} \sum_{SS'} X_S^{ft'} C_{SS'}^{-1} X_{S'}^{\nu t'} \tag{3.44}$$

t, t' and f all represent internal templates. This system is solved by inverting M_{tf}, and solving for the vector containing the coefficients $\tilde{c}_t^{\nu}$.

The actual implementation of the WI-FIT algorithm was done with computer-code written by my supervisor Frode K. Hansen. 500 Monte Carlo CMB-simulations were created for each band, with $N_{side} = 256$. The simulated CMB-maps were convolved with the WMAP-beams, and instrumental noise based on the standard deviation defined by the WMAP-instrument were added. Then a set of foreground templates were added, both the HFF-set(2.8.1) and the NFG-set were used to investigate the efficiency of the method.
After then removing the band-specific beams, the complete skymaps were all convolved with a common gaussian beam with $FWHM = 200$ arcminutes.
As mentioned in section 2.8.3, WI-FIT is biased due to the noise properties of both frequency-maps used in creating a template, being carried over to the template. Using such a large beam helps in alleviating this problem, it also turns out choosing the correct templates can reduces the noise.
We know that we need to create the same number of internal templates as there are distinct types of foreground-emission. Along with every internal template we choose, we need a coefficient. One template consists of the difference between

two frequency-bands, for instance K-Ka. So how do we choose which internal templates, or difference maps to use? Since we operate with three distinct foreground emission sources, we need three internal templates to clean each band. When we create the difference-maps, we get a noise-contribution from both that is included in the final, cleaned map. Since we want this noise-contribution to be as small as possible, it makes sense to want the coefficients we multiply the internal templates with, to be as small as possible. Using equations 3.36 and 3.38, we can write

$$\sum_{\nu\nu'} \tilde{c}^b_{\nu\nu'} \sum_f (c^\nu_f - c^{\nu'}_f) F^f = \sum_f c^b_f F^f \tag{3.45}$$

since the two different ways of representing the complete skymaps must necessarily be equal. b, ν and ν' represent frequency, with the condition $b \neq \nu \neq \nu'$. b is the band to be cleaned, ν and ν' are the bands that forms the templates. F is the foreground-components, with the sums running over types of foreground, or equivalently the number of internal templates.
Thus, we have a connection between the old, ETF-coefficients (c^b_f) and our new WI-FIT coeffiecients ($\tilde{c^b_{\nu\nu'}}$).
Equation 3.45 can be solved as simple matrix-equation. For cleaning each band, there are 4 remaining bands from which to form internal templates. For example, if we wish to clean the V-band, we can form internal templates by using the K, Ka, Q and W-bands. This means there will be

$$\binom{4}{2} = 6 \tag{3.46}$$

different combinations for each band. For instance, for the V-band, the possible combinations are K-Ka, K-Q, K-W, Ka-Q, Ka-W and Q-W. From such a set there are

$$\binom{6}{3} = 20 \tag{3.47}$$

different ways of selecting 3 templates. Solving equation 3.45, we looked for the sets of coefficients $\tilde{c}^b_{\nu\nu'}$ that had the smallest absolute value to minimize the amount of noise in our cleaned maps. The templates chosen are given in table 3.2. This selection differs somewhat from those chosen in [23].
It should be noted, due to time constraints we only did this analysis for the HFF-templates, and used the same internal template-combinations for the NFG-templates. Thus, the noise and bias for the latter may not have been minimized to the same degree of accuracy as with the HFF-templates.

Band	Template 1	Template 2	Template 3
Q	K-Ka	Ka-V	W-V
Va	K-Q	K-W	Ka-Q
W	K-Ka	Ka-Q	Q-V

Table 3.2: WIFIT templates

Using these templates, 3.42 is solved, and the Q-,V- and W-bands are cleaned through a linear combination of the templates and the calculated coefficients. The coefficients found for the W-band, fitting the templates in column 4 in table 3.2 were so large however, that the noise introduced in the simulated maps made them unsuitable for analysis.
[23] details a bias correction procedure that can be implemented in lieu of a large beam, to allow for higher detail and resolution in the cleaned maps, but this approach lies beyond the scope of this thesis.

Chapter 4

Results

The effectiveness of the cleaning will be assessed chiefly through calculating the direction of the quadru- and octopole and comparing results for the cleaned maps with those from the original simulated CMB-maps. This direction is calculated using polar coordinates (θ, ϕ). However, we only plot the θ direction.
If we look at a map, for instance 4.1,
the θ-direction corresponds to up-down(north/south), while ϕ corresponds to left-/right (east/west). Since the galaxy runs along the entire left/right direction(ϕ), but only covers a small band in the up/down (θ) direction, we make the assumption that the galaxy have a stronger impact on the direction of the multipoles in the θ-direction.
We also conduct a visual inspection of the maps, looking for residual foregrounds and noise.

4.1 ETF

For the ETF-implementation, we clean the Q-, V- and W-band, using 500 simulations for each band. The whole process is done twice, applying first the HFF-templates, then the NFG-set as a galactic foreground-model. To clean the map, the HFF-set is subtracted in both instances, using the coefficients derived from the χ^2-minimization.
The results presented are for the V-band. The results from the Q and W-bands are almost identical to those shown, so they have not been included.

Figure 4.1: ETF-cleaned V-band using HFF-templates

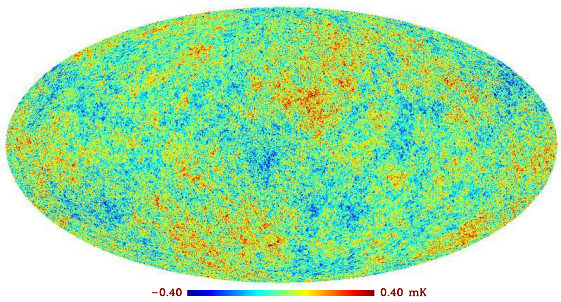

Simulated CMB-map

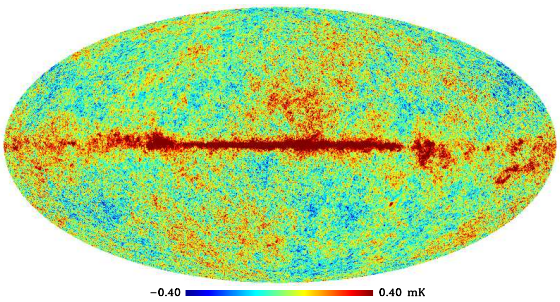

With foregrounds

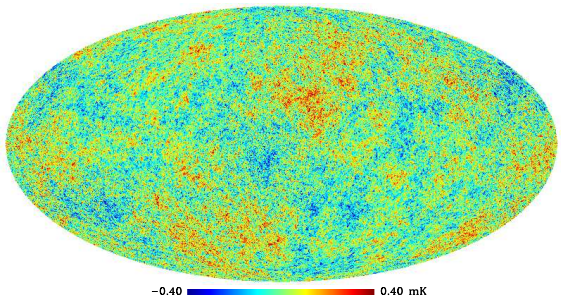

Cleaned map

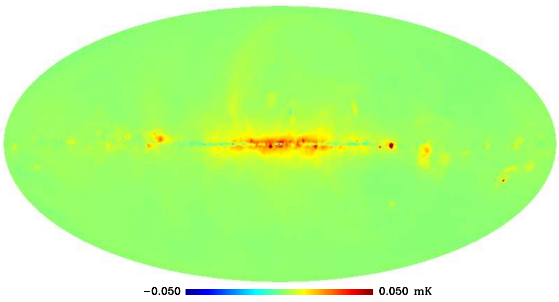

Difference between cleaned and simulated

The maps(figure 4.1) are shown at three different stages of the algorithm, the simulated map with instrumental noise added, the same map after the HFF-templates have been added, and finally the cleaned map. Also included is the difference between the cleaned and simulated map, note the different scale in the last display. In figure 4.2, the θ-direction of the quadru and octopole at two differ-

ent stages are plotted, the plots on the left showing the simulated CMB map versus the same map with foreground templates applied, the plots on the right showing the simulated CMB-map versus the cleaned map. The leftmost plots show how the foregrounds distort the measurements of the multipoles direction, while the rightmost plot tells us how effective the cleaning has been. A perfect result would have left all the points lying on a diagonal line.

Figure 4.2: ETF plots V-band using HFF-templates

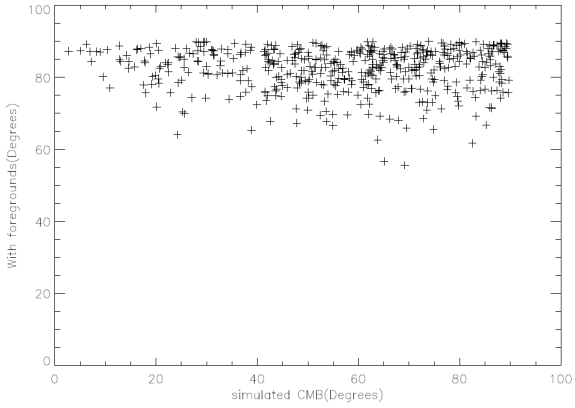

Full map quadrupole direction

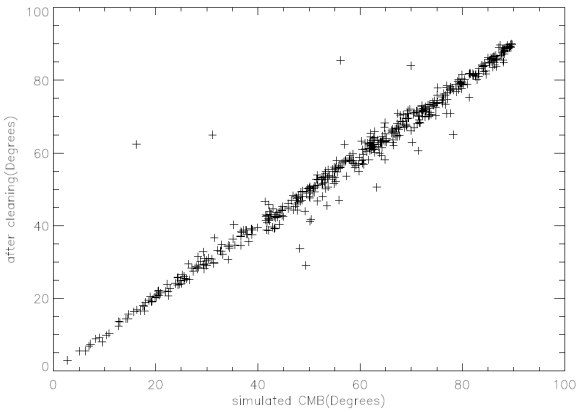

Cleaned map quadrupole direction

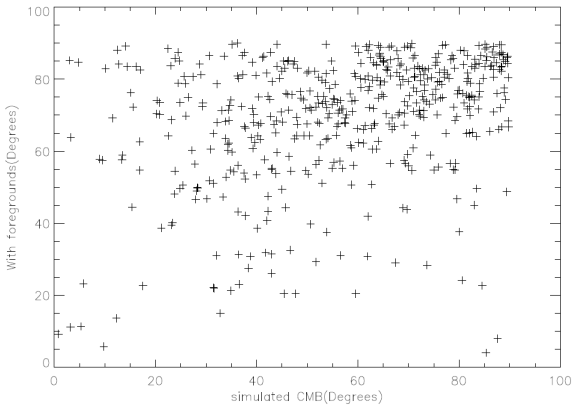

Full map octopole direction

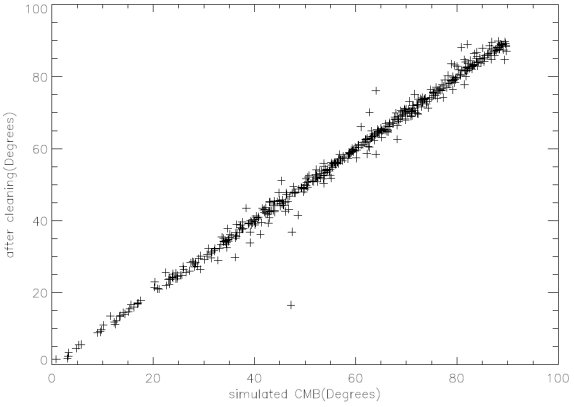

Cleaned map octopole direction

In tables 4.1 and 4.2, the angular distance $\Delta\Theta$ between the multipoles before (θ_1, ϕ_1) and after cleaning (θ_2, ϕ_2) is displayed, this is calculated through

$$\Delta\Theta = cos^{-1}\left(cos(\theta_1)cos(\theta_2) + sin(\theta_1)sin(\theta_2)cos(\phi_q - \phi_2)\right) \tag{4.1}$$

The values shown are the mean values over 500 simulations.

$Band$	$\Delta\Theta$ with fg	$\Delta\Theta$ after cleaning
Q	79.628	3.446
V	65.115	3.895
W	71.053	3.121

Table 4.1: ETF mean angular distance, quadrupole, HFF-templates

$Band$	$\Delta\Theta$ with fg	$\Delta\Theta$ after cleaning
Q	74.486	3.064
V	63.046	2.495
W	68.219	2.379

Table 4.2: ETF mean angular distance, octopole, HFF-templates

Moving on to the NFG foreground templates, results for the Q and V-bands are shown, results for W are almost identical to V. Keep in mind that it is still the *HFF-templates* that are used to **clean** the maps.

Figure 4.3: ETF-cleaned Q-band with NFG foregrounds

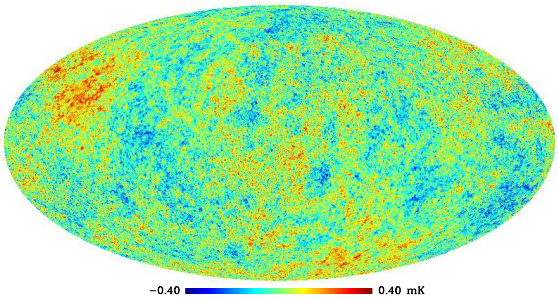

Simulated CMB-map

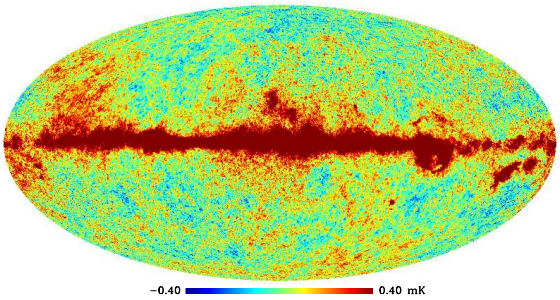

With foregrounds

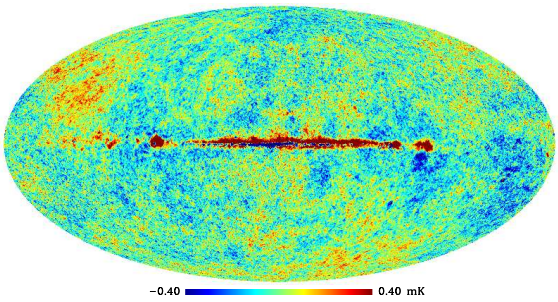

Cleaned map

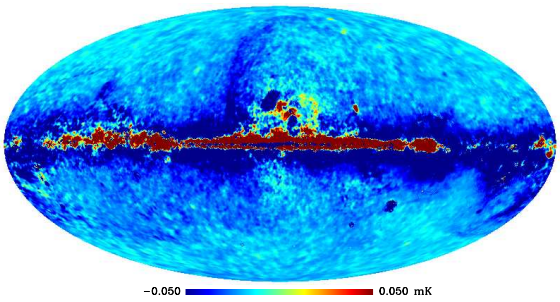

Difference between cleaned and simulated

Figure 4.4: ETF plots Q-band with NFG foregrounds

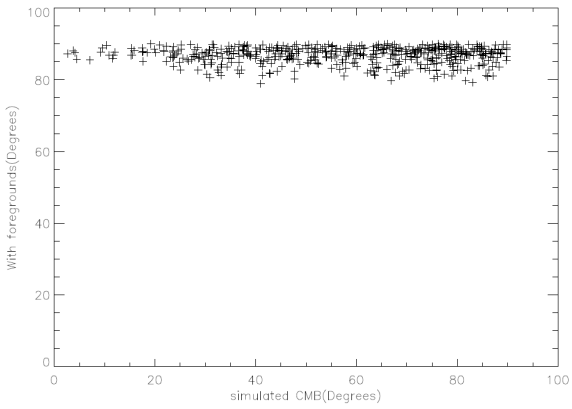

Full map quadrupole direction

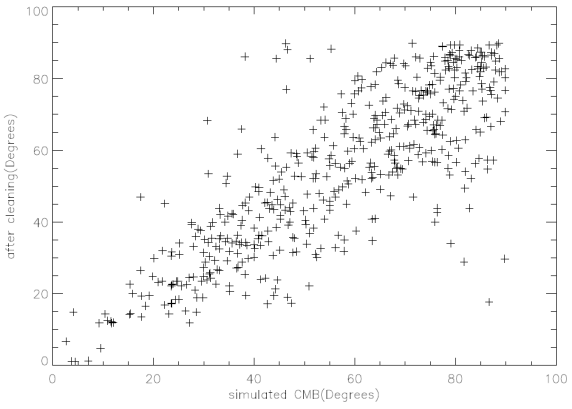

Cleaned map quadrupole direction

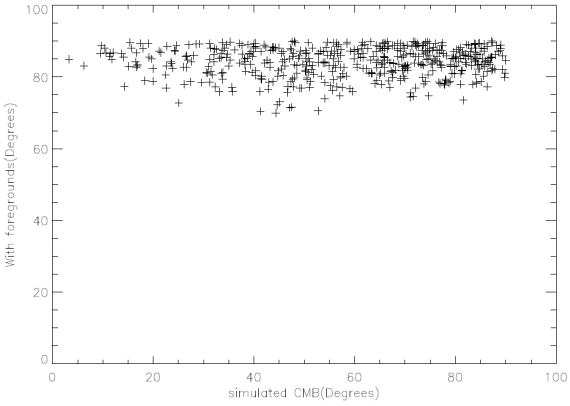

Full map octopole direction

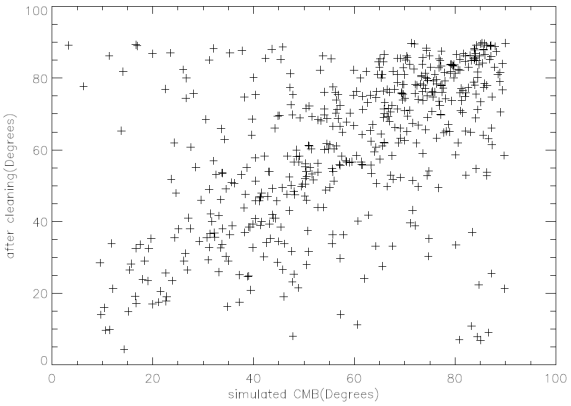

Cleaned map octopole direction

Figures 4.3 and 4.4, showing results from the Q-band show a clear deterioration when compared to results for the HFF-templates. Since the NFG-templates includes variations in the spectral index across the sky, it is no surprise that the cleaning does poorly close to the galactic plane since the HFF-templates assumes constant spectral indexes. In accordance with figure 2.13, we know there are more foreground contamination present in the Q-band than in V or W. The V-band results (figures 4.6 and 4.5) are much better, and the W-band even better. The V-band is shown in the interest of comparison with results for WI-FIT, where the W-band

are not usable. For ETF, the W-band results are actually better than for the V-band.

Figure 4.5: ETF-cleaned V-band with NFG foregrounds

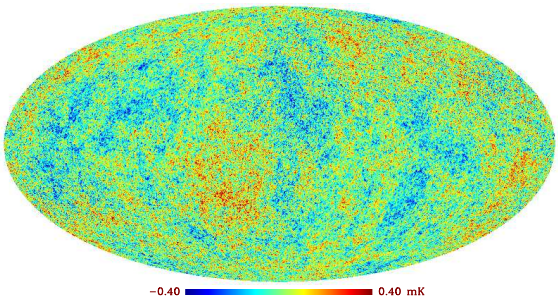

Simulated CMB-map

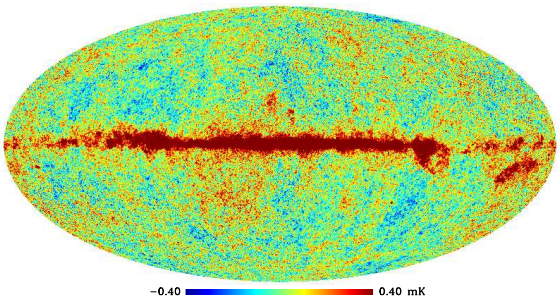

With foregrounds

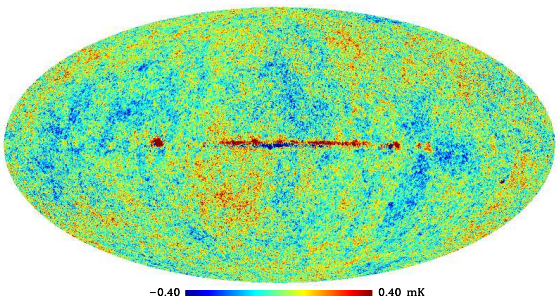

Cleaned map

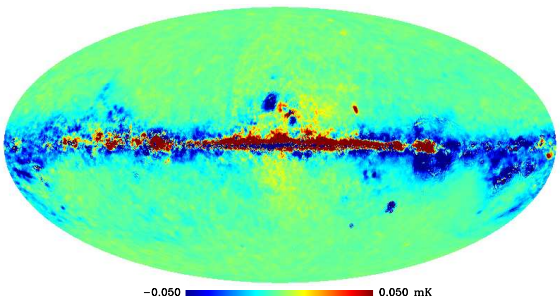

Difference between cleaned and simulated

Figure 4.6: ETF plots V-band with NFG foregrounds

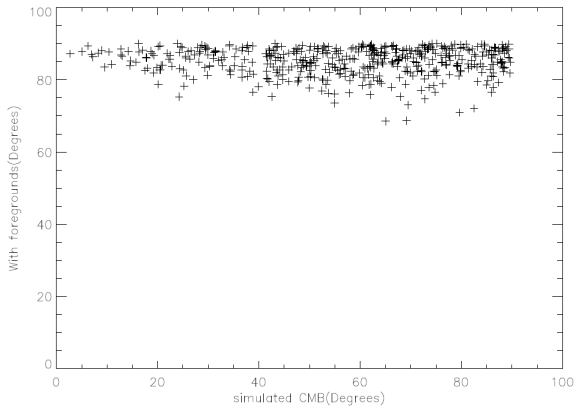

Full map quadrupole direction

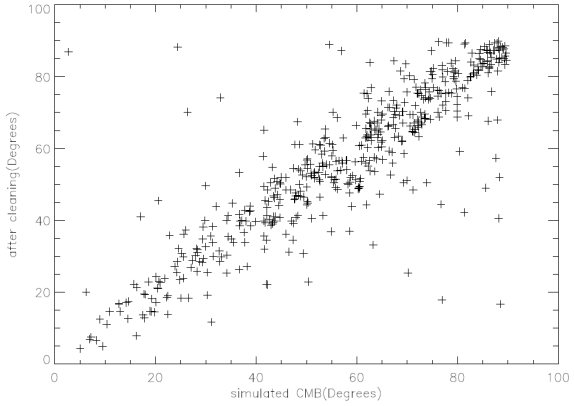

Cleaned map quadrupole direction

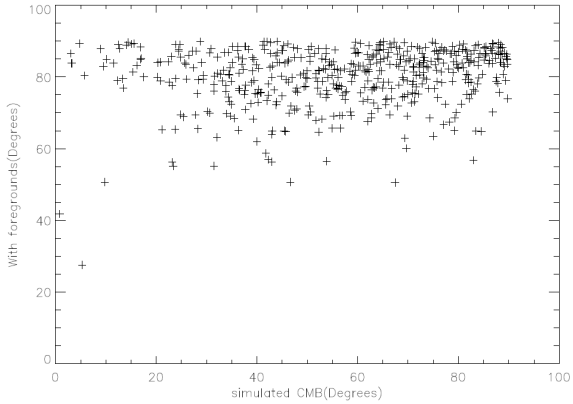

Full map octopole direction

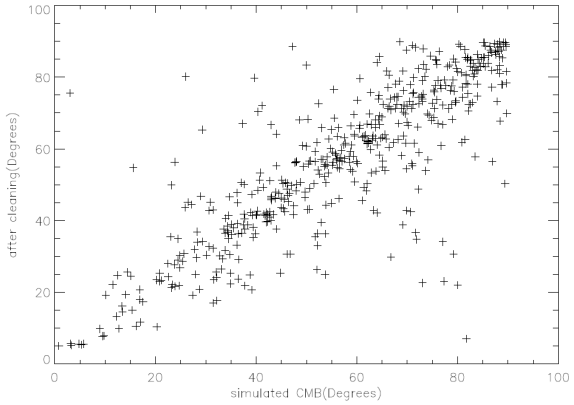

Cleaned map octopole direction

Tables 4.3 and 4.4 show the distance between the multipoles, displaying the poor performance of the Q-band.

$Band$	$\Delta\Theta$ with fg	$\Delta\Theta$ after cleaning
Q	85.243	28.204
V	75.425	18.460
W	76.766	14.168

Table 4.3: ETF mean angular distance, quadrupole, NFG foregrounds

$Band$	$\Delta\Theta$ with fg	$\Delta\Theta$ after cleaning
Q	79.882	36.087
V	75.417	20.971
W	77.429	14.215

Table 4.4: ETF mean angular distance, octopole, NFG foregrounds

The above is all done with the maps smoothed by beams defined by the parameters of the WMAP satellite. For purposes of comparing results with those from WI-FIT, we also applied a large beam ($200'$), along with the NFG foregrounds. Here we show the results for the V-band, as this is the most important result for comparison with WI-FIT.

Figure 4.7: ETF-cleaned V-band with NFG foreground, large beam

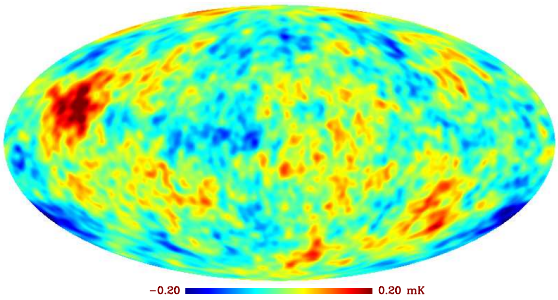

Simulated CMB-map

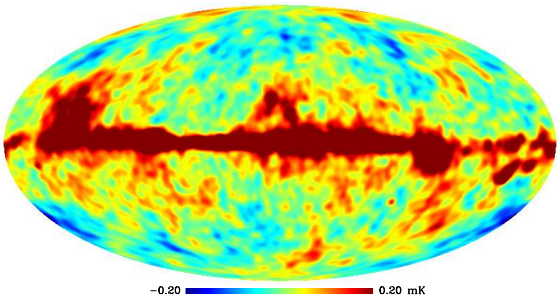

With foregrounds

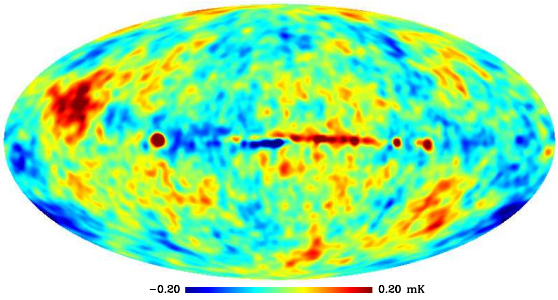

Cleaned map

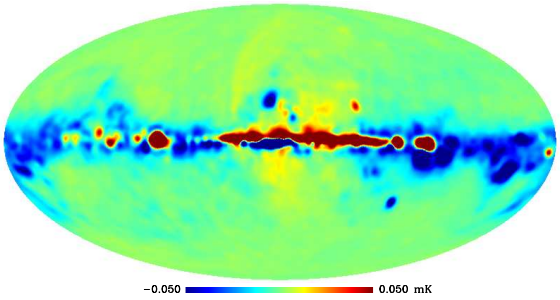

Difference between cleaned and simulated

Figure 4.8: ETF plots V-band with NFG foregrounds, large beam

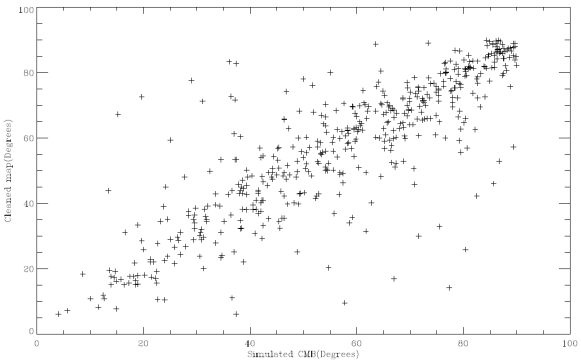

Quadrupole

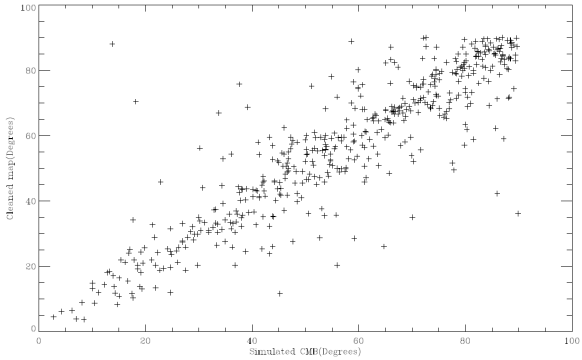

Octopole

These results are quite good, and tables 4.5 and 4.6 show the large beam to have had a minimal impact on the final results.

Band	$\Delta\theta$ with fg	$\Delta\theta$ after cleaning
Q	86.478	36.499
V	73.485	18.738
W	76.765	13.205

Table 4.5: ETF mean angular distance, quadrupole, large beam

Band	$\Delta\theta$ with fg	$\Delta\theta$ after cleaning
Q	87.485	36.548
V	75.012	20.152
W	76.712	14.863

Table 4.6: ETF mean angular distance, octopole, large beam

Finally, the WMAP datamaps are cleaned using HFF-templates along with the coefficients calculated by simulations using the same templates. As expected, the results close to the galactic plane are poor, and masks needs to be applied for these maps to be useful for cosmological analysis. In these maps, we find a

distance between the quadru and octopole directions of 50° or more, which only underlines the inadequacy of this approach when applied to the full sky.

Figure 4.9: WMAP cleaned with ETF

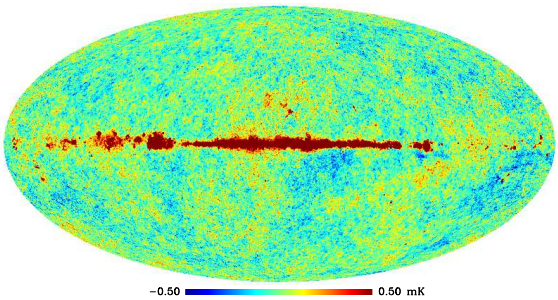

Q-band

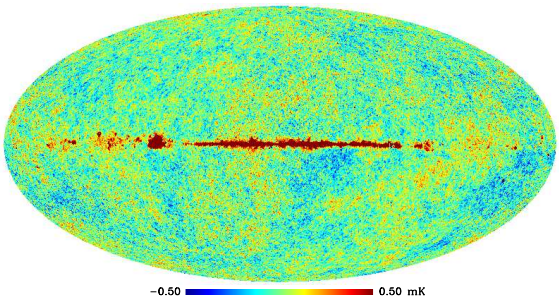

V-band

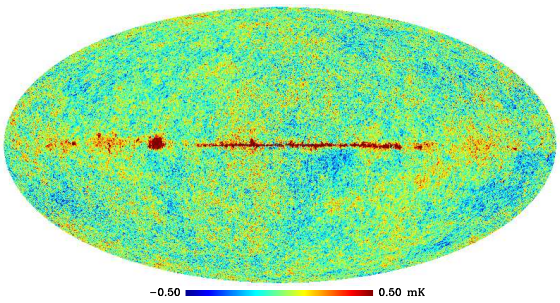

W-band

4.2 ILC

ILC uses a linear combination of all five frequency-bands, there are therefore no band-specific results. 500 simulations were done, again in two separate instances using the HFF- and the NFG-templates. The maps are shown in figures 4.10 and 4.12 for HFF and NFG respectively.
Changes in the θ-component of the multipole-directions are shown in figure 4.11. The performance with the HFF-templates are better than those using the NFG foregrounds, as was to be expected. The varying spectral index in the latter will cause more uncertainties in the results close to the galactic plane. Nevertheless, ILC performs well when compared to ETF, the final distortion in the multipole directions being almost identical between the two methods when looking at the results using NFG-templates.
Tables 4.7 and 4.8 confirms this, with $\delta\theta$-values comparable to ETF. It is worth remembering it is possible to divide the sky into smaller parts to account for changes in the spectral index, ILC has been proven to give even better results with such an approach [10].

Figure 4.10: ILC-simulations using HFF

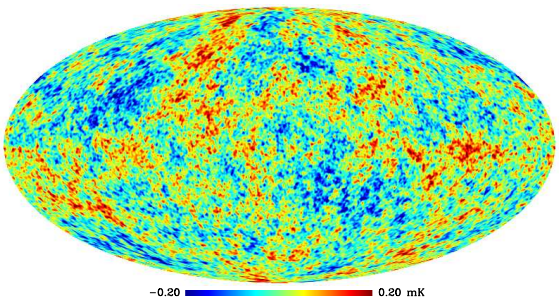

Simulated map

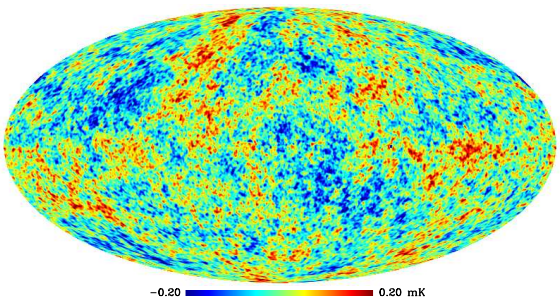

Cleaned map

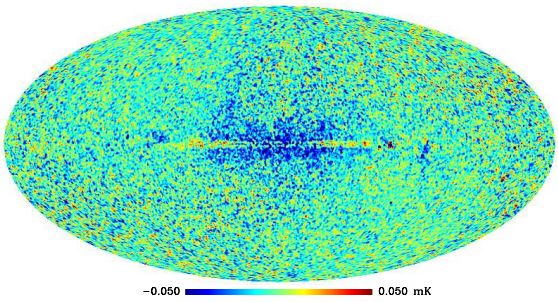

Difference map for 1 simulation

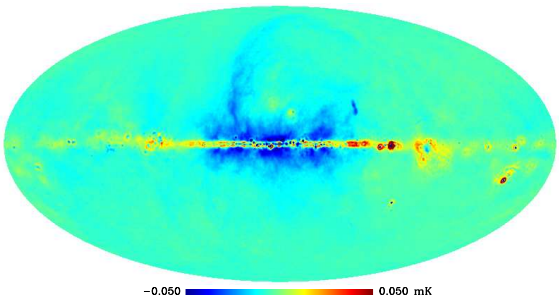

Average difference map for 500 simulations

Figure 4.11: ILC plots

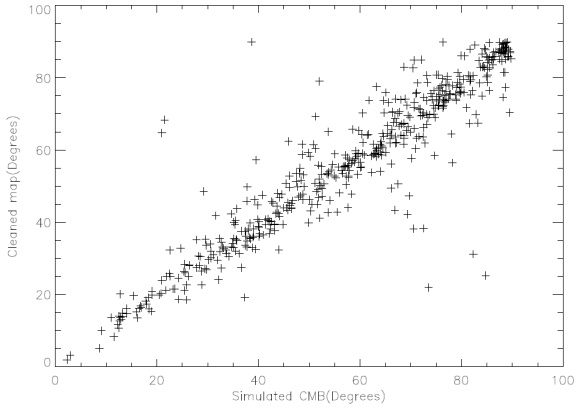

Direction of quadrupole
simulated vs. cleaned map, HFF templates

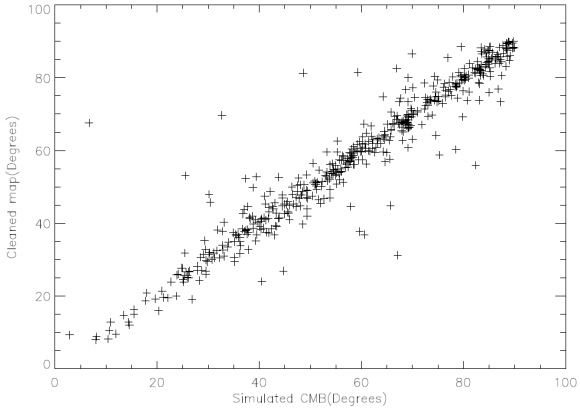

Direction of octopole
simulated vs. clean map, HFF, templates

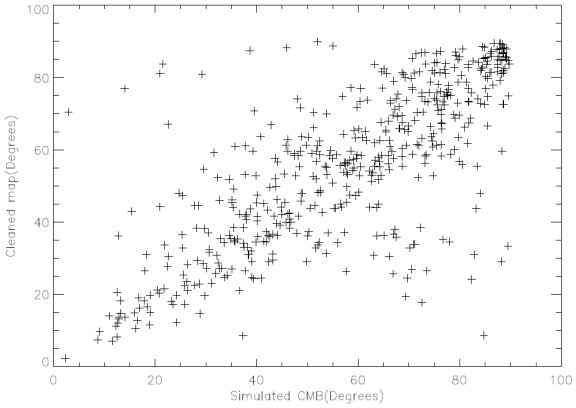

Direction of quadrupole
simulated vs. cleaned map, NFG templates

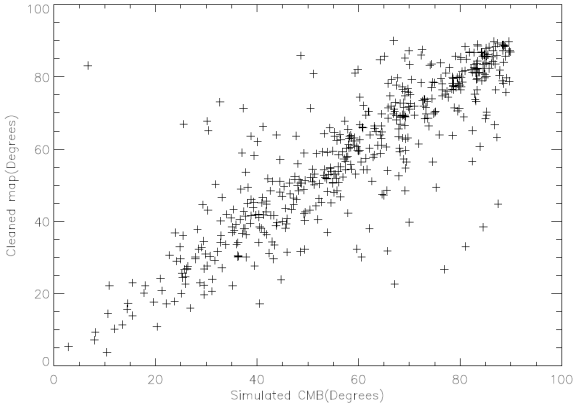

Direction of octopole
simulated vs. clean map, NFG templates

Multipole	$\Delta\Theta$ after cleaning
Quadrupole	12.995
Octopole	10.157

Table 4.7: ILC mean angular distance

Multipole	$\Delta\Theta$ after cleaning
Quadrupole	26.279
Octopole	19.951

Table 4.8: ILC mean angular distance, NFG foregrounds

Figure 4.12: ILC-simulations using NFG foregrounds

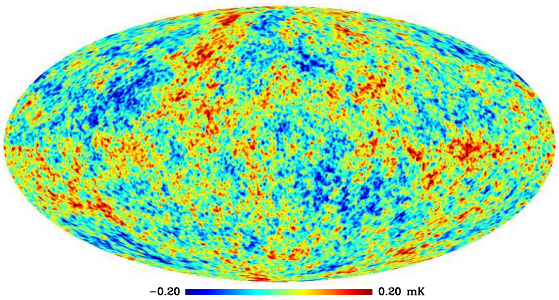

Simulated map

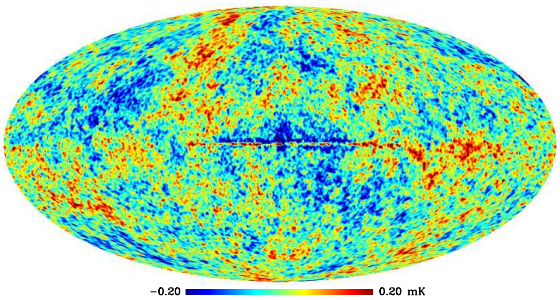

Cleaned map

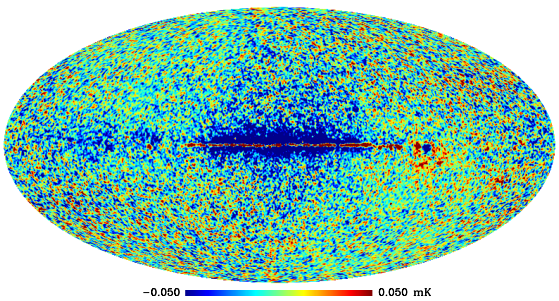

Difference map for 1 simulation

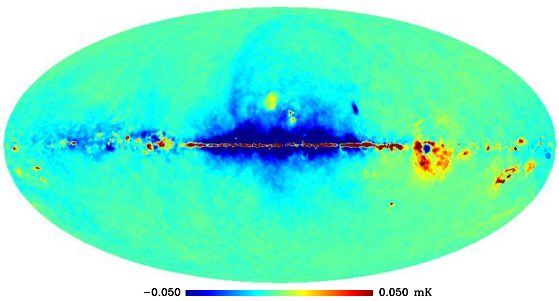

Average difference map for 500 simulations

As we did with the ETF-method, we have applied a larger beam for sake of comparison with WI-FIT results. Perhaps the biggest drawback of the ILC-method, is the complicated noise properties. A large beam will serve to suppress noise on smaller scales, and we can therefore expect ILC-results to improve using such a large beam. As figure 4.14 and table 4.9 shows, this is exactly what happens. Results are now comparable to those achieved using the HFF-templates that have constant spectral indexes.

Figure 4.13: ILC-simulations, using NFG templates and large beam

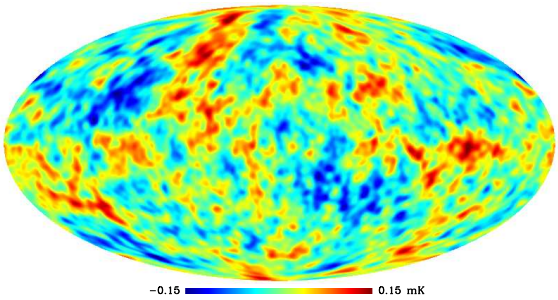

Simulated map

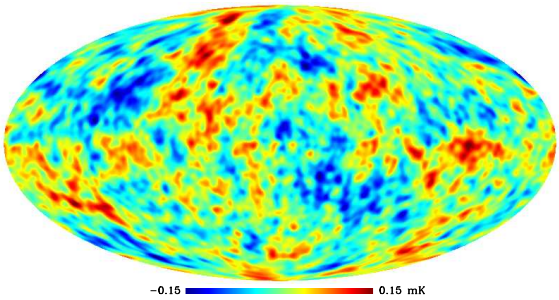

Cleaned map

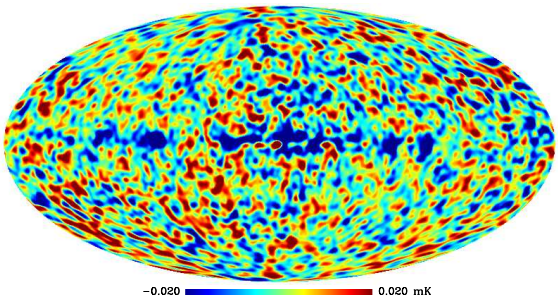

Difference map for 1 simulation

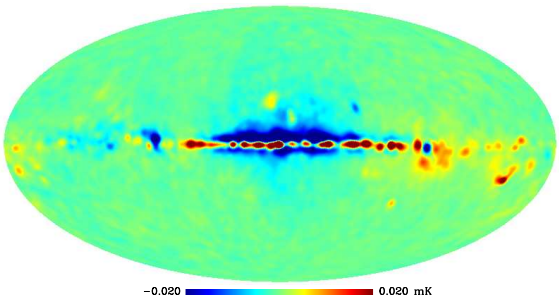

Average difference map for 500 simulations

Figure 4.14: ILC-simulations, using NFG templates and large beam

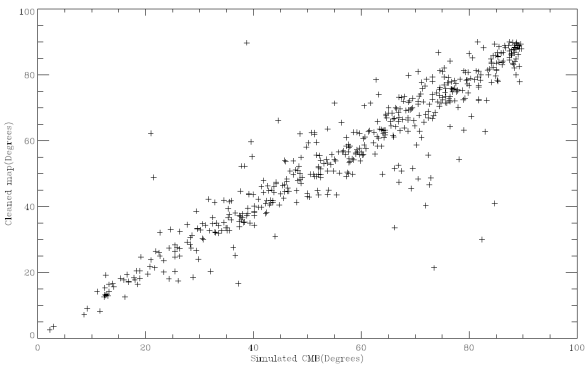

Direction of quadrupole
simulated vs. cleaned map

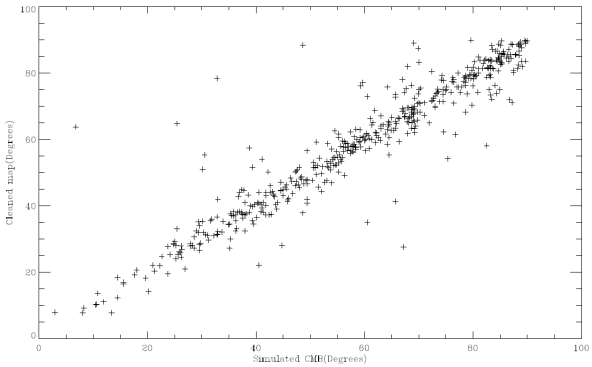

Direction of octopole
simulated vs. clean map

Multipole	$\Delta\Theta$ after cleaning
Quadrupole	10.582
Octopole	11.622

Table 4.9: ILC mean angular distance, large beam

The ILC-algorithm has also been applied to the WMAP-data. the result being shown in figure 4.2. By visual inspection, this seems to have been more successful than the ETF-approach.

Figure 4.15: ILC-method, applied to WMAP-data

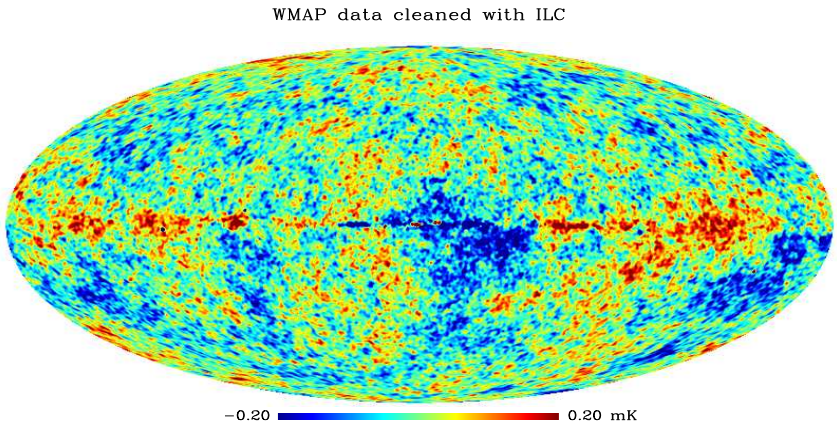

Finally, in table 4.10 we have listed the weights found for the internal combinations. While these may not be particularly informative, they are included for completeness.

Set	K	Ka	Q	V	W
HFF foregrounds	0.02131	-0.72117	1.32333	0.17831	0.19822
NFG foregrounds	0.04528	-0.92887	0.52262	2.24299	-0.88202
NFG foreground,large beam	0.42836	-2.24412	0.92653	3.17574	-1.28652
WMAP data	-0.00995	-0.18123	-0.34255	1.46649	0.06724

Table 4.10: ILC weights, mean over 500 simulations

4.3 WI-FIT

The WI-FIT algorithm was also applied to 500 simulations. Due to the bias inherent in the method, we only present results for the V-band as they are the cleanest

and least disturbed by bias. The large beam, of $FWHM = 200'$ is applied to minimize the bias, but our results show even this is insufficient to avoid bias in the Q and especially the W-band.

Figure 4.16: WIFIT-cleaned V-band, HFF

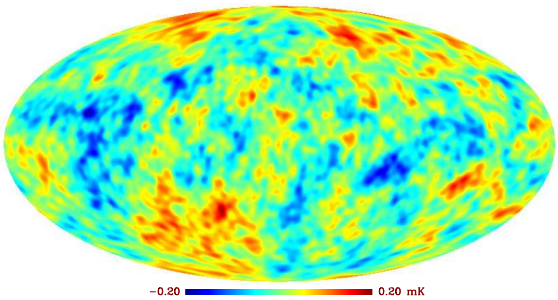

Simulated map

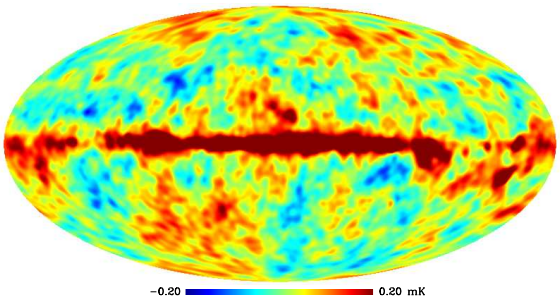

With foregrounds

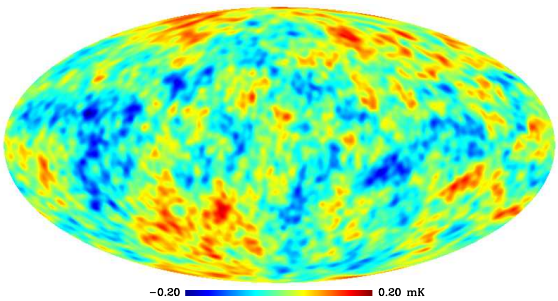

Cleaned map

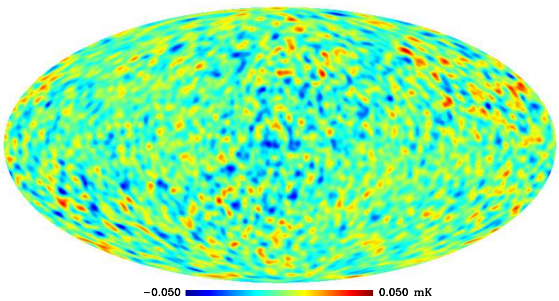

Difference between cleaned and simulated

Figure 4.17: WIFIT plots V-band, HFF

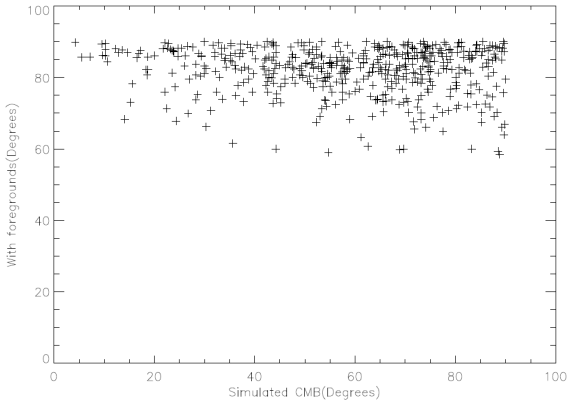

Full map quadrupole direction

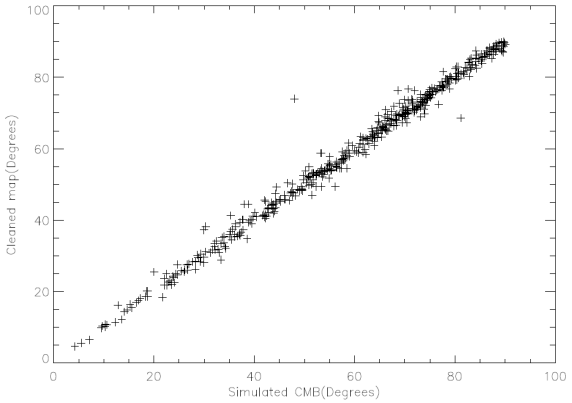

Cleaned map quadrupole direction

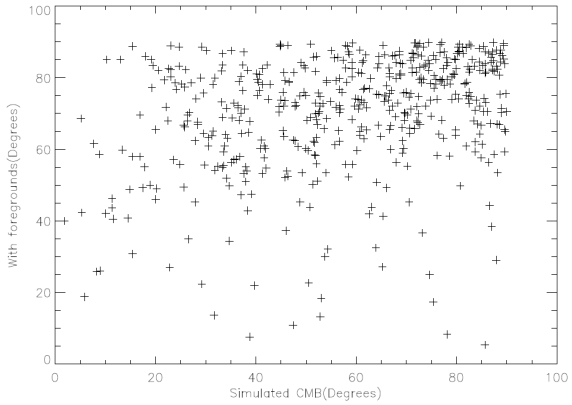

Full map octopole direction

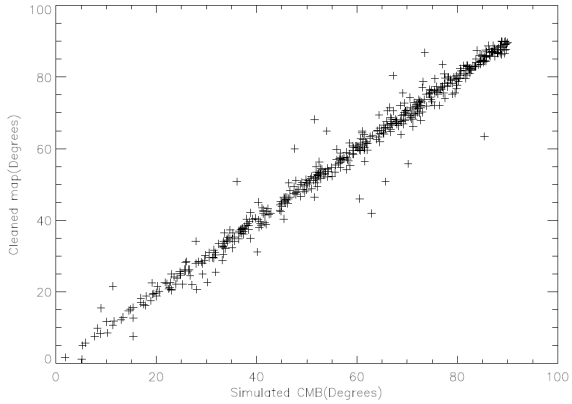

Cleaned map octopole direction

Aa these plots show, WI-FIT does exceptionally well when dealing with the HFF-foregrounds. These results are an almost perfect match for those achieved using ETF. Looking at tables 4.11 and 4.12, keep in mind only the V-band is of interest.

$Band$	$\Delta\Theta$ with fg	$\Delta\Theta$ after cleaning
Q	74.505	25.937
V	65.716	3.440
W	70.048	17.677

Table 4.11: WIFIT mean angular distance, quadrupole, HFF

$Band$	$\Delta\Theta$ with fg	$\Delta\Theta$ after cleaning
Q	79.384	24.638
V	65.598	5.107
W	69.211	22.964

Table 4.12: WIFIT mean angular distance, octopole, HFF

Moving on the NFG-templates, the results are not nearly as good. WI-FIT appears more sensitive to changes in the spectral index, and the residual remains of foreground contamination after cleaning renders the maps unsuited for cosmological analysis without applying masks to avoid those areas of the sky most contaminated by foregrounds.

Figure 4.18: WIFIT-cleaned V-band, NFG foregrounds

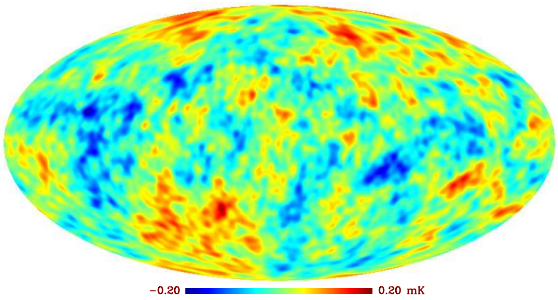

Simulated map

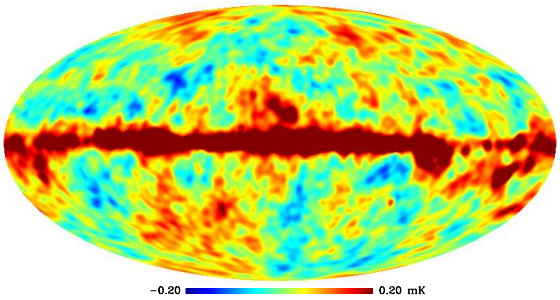

With foregrounds

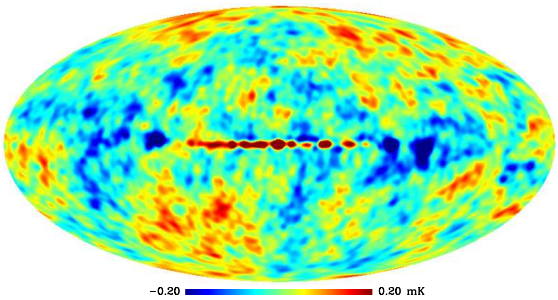

Cleaned map

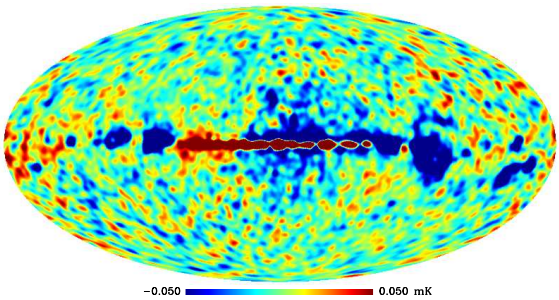

Difference between cleaned and simulated

Figure 4.19: WIFIT plots V-band, NFG foregrounds

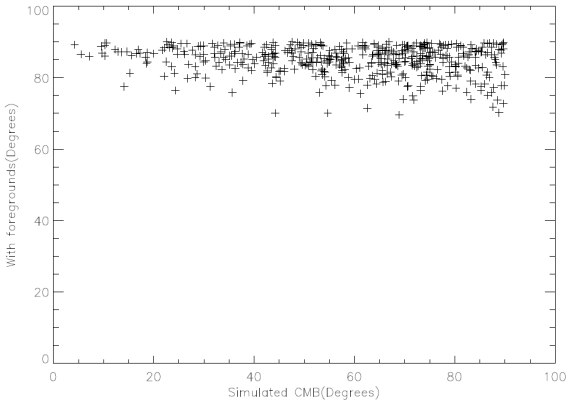

Full map quadrupole direction

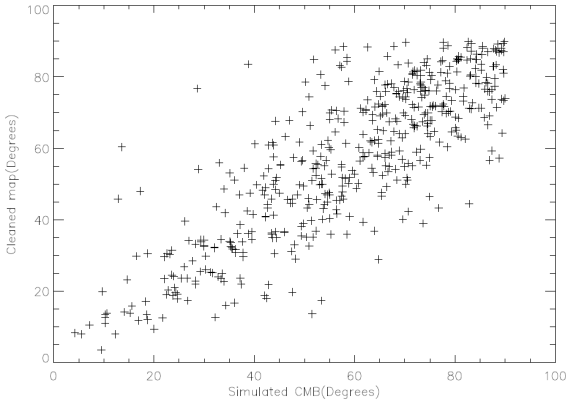

Cleaned map quadrupole direction

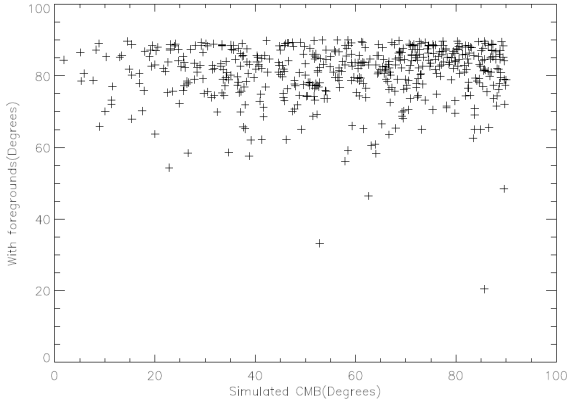

Full map octopole direction

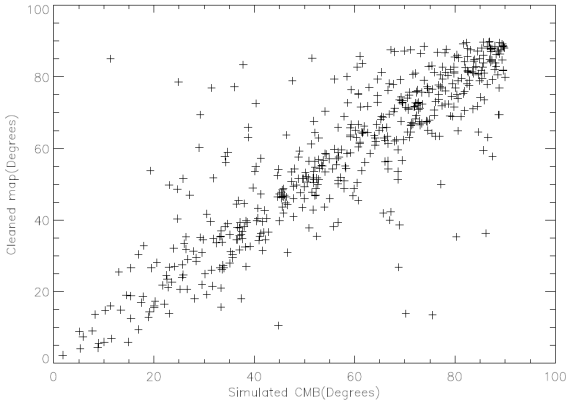

Cleaned map octopole direction

Confirming the plots above, tables 4.13 and 4.14 shows WI-FIT can not accurately reproduce the simulated CMB-maps.

Band	$\Delta\Theta$ with fg	$\Delta\Theta$ after cleaning
Q	81.997	49.662
V	74.021	29.417
W	75.627	38.103

Table 4.13: WIFIT mean angular distance, quadrupole, NFG foregrounds

Band	$\Delta\Theta$ with fg	$\Delta\Theta$ after cleaning
Q	87.097	35.939
V	79.382	21.986
W	78.349	29.414

Table 4.14: WIFIT mean angular distance, octopole, NFG foregrounds

In figure 4.20, we have plotted the distance between the quadru- and octopoles, simulated maps vs. cleaned maps for all three methods with the NFG templates and large beam applied. As mentioned in section 2.6, this distance is very small in the WMAP-data, 7° according to [10]. As the figure shows, it seems unlikely that this is caused by foreground contamination, since none of the methods applied shows signs of decreasing the distance between the two multipoles. Also worth noticing is just how unlikely it is that that distance should be zero in the first place, a quick visual inspection shows there are about 11 out of 1500 simulations where the distance is below 7° in these plots.

Figure 4.20: Angular distance between quadru- and octopole

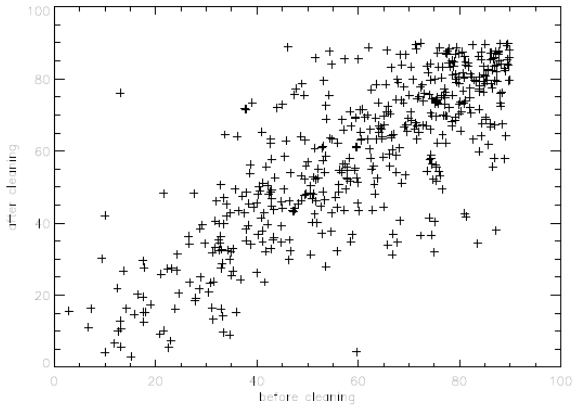

External Template Fitting

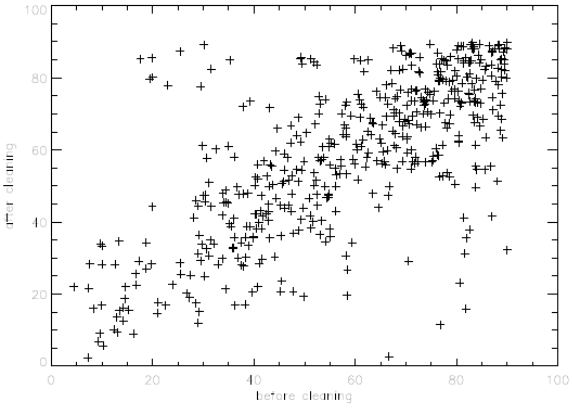

Internal Linear Combination

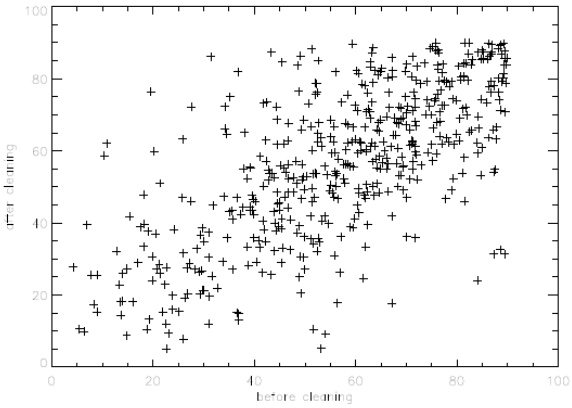

WI-FIT

Chapter 5

Discussion

We have used three different methods of removing foreground contamination from simulated skymaps, investigating the impact of the cleaning techniques on the direction of the quadru- and octopole.
We have used two different sets of templates to model the galactic component of the foreground emissions.

Looking at the External Template Fitting (ETF)-results first, using the HFF-templates yields almost perfect cleaning. The directions of the two multipoles in question change by only a miniscule amount ($\sim 3°$) after foregrounds have been added and then removed. This is not a particularly telling result however, since we are subtracting the same templates we added as foregrounds.
Moving on to the NFG-templates, the results are more interesting. The Q-band appears unsuitable for cosmological analysis, the directions of the two multipoles deviating significantly between the simulated and cleaned maps. We have found an average difference of roughly $30°$ in the θ-direction for this band. From figure 2.13 we know the Q-band contains more foreground contamination than the other two bands, which will make this band harder to clean, regardless of the method applied. The V- and W-bands perform adequately well, both with the high-resolution WMAP-beams and when convolved with a $200'$ beam.
For these bands we find an average distortion between $15°$ and $20°$ both with and without the larger beam.

With regards to the ILC-simulations, results are slightly worse than ETF with both sets of templates. When using a linear combination of different frequency-maps, the instrumental noise from all different bands are included in the final map, al-

beit weighted. This complication puts ILC at a disadvantage when compared with ETF since the templates are noise-free, however as discussed in section 2.6, noise is primarily prevalent at smaller scales. By convolving with the $200'$ beam, the noise is largely suppressed, and the ILC-results improve, outperforming ETF.
The HFF-templates yields an average distance of roughly 10°. Applying the NFG-set, the mean distance jumps to a little over 20°. When convolving with the large beam ($200'$), our results are on the same level as those with the HFF-templates.

Moving on to WI-FIT, the performance with the HFF-templates are quite good, exceptionally so for the V-band with an average distance between the quadrupole in the simulated and cleaned maps of only 3°! The results with the NFG-templates however, are the worst amongst the three methods ($\sim 20^\circ$). The HFF-templates have a constant spectral index, while the NFG templates do not. It seems the WI-FIT method does not perform as well as the other two methods when dealing with varying spectral indexes across the sky, *when the method is applied to the full sky*. This is probably due in part to the bias introduced by ignoring the noise-component in the internal templates when we calculate the coefficients. As mentioned, [23] details a bias-correction procedure, that we have not made use of in this thesis.

To achieve better results, the sky can be divided into smaller parts, and the cleaning algorithm applied separately to each one. This approach has already been applied to the ILC-method [10]. [23] warns that applying the method to smaller patches of the sky would mean an even more complicated noise structure, obscuring smaller scales.

Two of the algorithms have also been tested on the datamaps.
When subtracting the HFF-templates from the WMAP data, ETF performs poorly in the galactic plane. This is to due to the template set not taking into account the variation in spectral indexes.
ILC gives a much more satisfying visual result, but foreground residuals are still apparent in the galactic plane. This method has also been successfully applied to smaller regions of the sky separately, improving results further.
Unfortunately, there was not enough time for testing the WI-FIT algorithm on the WMAP data.

Inflation theory predicts that the CMB should exhibit B-mode polarization, the

Planck satellite is expected to produce data suitable for testing this prediction. However, no external templates of galactic polarization exist. It is therefore vital that methods using only internal data are developed to study the CMB-polarization. From our results, we can conclude ILC performs better when applied to the full sky than WI-FIT, but a better test of the respective methods performance would be to divide the sky into smaller patches, and apply the cleaning-algorithms to each patch individually. This way, the errors induced by assuming constant spectral indexes would be limited by the size of the patch.
By comparing results from WI-FIT with those from ETF, we see an exceptional performance from WI-FIT when we use the HFF-templates, which assumes a constant spectral index. ILC on the other hand, does not do as well. It seems reasonable then, to expect WI-FIT to match, or even out-perform ILC when looking at small partitions of the sky where the spectral index will not vary much.

For the actual measurements of the directions of the quadru- and octopole, our simulations indicate the ILC with a large beam gives the most accurate results. However, it is not so much the direction itself that is of interest, but rather the impact of foregrounds and the three cleaning methods on that measured direction. Looking at figure 4.20, we see no indication that the different algorithms *decrease* the distance between the two multipoles, though the spread in the plots are too large to completely rule out a foreground-related cause for the alignment.

5.1 Future Work

There are several things that could be done to improve upon the analysis done here.

- Bias-correction in the WI-FIT algorithm. To minimize bias, we have used a very large beam, which results in a loss of information on smaller scales.
- Apply the ILC-algorithm to a partitioned sky. This will lead to better results in the galactic plane, where there is much variation in the spectral indexes.
- Apply the WI-FIT algorithm to a partitioned sky. Our results using the HFF-templates indicates this should substantially improve results.
- Apply masks to those areas most affected by galactic contamination. Our analysis tends to be dominated by what happens in the central galactic plane, using masks would produce results that were more dependent on how the cleaning algorithms perform *outside* the galaxy, which might lead to different conclusions. Masking parts of sky may also give 'false' detections of the multipole directions, if large parts of the power of those multipoles happen to be located in the part of the sky we mask.

Bibliography

[1] R.A. Alpher, H. Bethe, and G. Gamow. The origin of chemical elements. *Physical Review*, 73, 1948.

[2] C.L. Bennett, R.S. Hill, G. Hinshaw, M.R. Nolta, N. Odegard, L.Page, D.N. Spergel, J.L. Weiland, E.L. Wright, M. Halpern, N. Jarosik, A.Kogut, M. Limon, S.S. Meyer, G.S. Tucker, and E. Wollak. First year wilkinson microwave anisotropy probe (wmap) observations: Foreground emission. *ApJ*, 148, 2003.

[3] B.Gold, C.L.Bennett, R.S.Hill, G.Hinshaw, N.Odegard, L.Page, D.N.Spergel, J.L.Weiland, J.Dunkley, M.Halpern, N.Jarosik, A.Kogut, E.Komatsu, D.Larson, S.S.Meyer, M.R.Nolta, E.Wollack, and E.L.Wright. Five-year wilkinson microwave anisotropy probe observations: Galactic foreground emission. *astro-ph*, 0803.0715, 2008.

[4] B.W. Carroll and D.A. Ostlie. *An Introduction to Modern Astrophysics*. Addison-Wesley, 1996.

[5] A. de Oliveira-Costa, M. Tegmark, M. Zaldarriaga, and A. Hamilton. The significance of the largest scale cmb fluctuations in wmap. *Phys.Rev*, 69, 2003.

[6] Scott Dodelson. *Modern Cosmology*. Academic Press, 2003.

[7] D.P.Finkbeiner, G.I.Langston, and A.H.Minter. Microwave interstellar medium emission in the green bank galactic plane survey: evidence for spinning dust. *ApJ*, 617, 2004.

[8] E.Hummel, M.Dahlem, J.M.van der Hulst, and S.Sukumar. The large-scale radio continuum structure of the edge-on spiral galaxy ngc891. *Astron.Astrophys.*, 246, 1991.

[9] Oystein Elgaroy. Ast4220: Cosmology 1 lecture notes, 2006.

[10] H.K. Eriksen, A.J. Banday, K.M. Górski, and P.B. Lilje. On foreground removal from the wmap data by an internal linear combination method: Limitations and implications. *ApJ*, 612, 2004.

[11] C. Watson et al. Planck surveyor. Planck homepage, 2007. http://www.rssd.esa.int/index.php?project=PLANCK&page=index.

[12] C.L. Bennett et al. Wilkinson microwave anisotropy probe. WMAP homepage, 2003. http://map.gsfc.nasa.gov.

[13] G. Smoot et al. Cosmic background explorer. COBE homepage, 1989. http://lambda.gsfc.nasa.gov/product/cobe/.

[14] Douglas P. Finkbeiner. A full-sky h-alpha template for microwave foreground prediction. *astro-ph*, 0301558, 2003.

[15] D.P. Finkbeiner, M. Davis, and D.J. Schlegel. Extrapolation of galactic dust emission at 100 microns to cmbr frequencies using firas. *ApJ*, 524, 1999.

[16] R.A. Freedman and W.J. Kauffman. *Universe, 6th edition*. W.H. Freeman and Company, 2001.

[17] G.Hinshaw, D.N.Spergel, L.Verde, R.S.Hill, S.S.Meyer, C.Barnes, C.L.Bennett, M.Halpern, N.Jarosik, A.Kogut, E.Komatsu, M.Limon, L.Page, G.S.Tucker, J.L.Weiland, E.Wollack, and E.L.Wright. First year wilkinson microwave anisotropy probe observations: The angular power spectrum. *ApJ*, 148, 2003.

[18] G.Hinshaw, J.L.Weiland, R.S.Hill, N.Odegard, D.Larson, C.L.Bennett, J.Dunkley, B.Gold, M.R.Greason, N.Jarosik, E.Komatsu, M.R.Nolta, L.Page, D.N.Spergel, E.Wollack, M.Halpern, A.Kogut, M.Limon, S.S.Meyer, G.S.Tucker, and E.L.Wright. Five-year wilkinson microwave anisotropy probe observations: Data processing, sky maps, & basic results. *astro-ph*, 0803.0732, 2008.

[19] R.C. Gonzalez and R.E. Woods. *Digital Image Processing(3rd edition*. Prentice Hall, 2007.

[20] K.M. Górski, E.Hivon, A.J.Banday, B.D.Wandelt, F.K.Hansen, M.Reinecke, and M.Bartelman. Healpix : a framework for high resolution discretization and fast analysis of data distributed on the sphere. *ApJ*, 622, 2004.

[21] K.M. Górski, E.Hivon, A.J.Banday, B.D.Wandelt, F.K.Hansen, M.Reinecke, and M.Bartelman. Healpix homepage. NASA Jet Propulsion Laboratory, 2004. http://healpix.jpl.nasa.gov/.

[22] K.M. Gòrski, G. Hinshaw, A.J. Banday, C.L. Bennett, E.L. Wright, A. Kogut, G.F. Smoot, and P. Lubin. On determining the spectrum of primordial inhomogeneity from the cobe dmr sky maps: Results of two-year data analysis. *astro-ph*, 9403067, 1994.

[23] F.K. Hansen, A.J. Banday, H.K. Eriksen, K.M. Górski, and P.B. Lilje. Foreground subtraction of cosmic microwave background maps using wi-fit. *ApJ*, 648, 2006.

[24] F.K. Hansen, A.J. Banday, and K.M. Gòrski. Testing the cosmological principle of isotropy: local power spectrum estimates of the wmap data. *astro-ph*, 0404206, 2004.

[25] C.G.T. Haslam, U. Klein, C.J. Salter, H. Stoffel, W.E. Wilson, M.N. Cleary, D.J. Cooke, and P. Thomasson. A 408 mhz all-sky continuum survey. *Astronomy and Astrophysics Supplement Series*, 47, 1981.

[26] R.M. Humphreys and J.A. Larsen. The sun's distance above the galactic plane. *Astronomical Journal*, 110, 1995.

[27] Kate Land and João Magueijo. The axis of evil. *Phys.Rev.Lett.*, 95, 2005.

[28] E. Martinez-Gonzalez, J.E. Gallegos, F. Argueso, L. Cayon, and J.L. Sanz. The performance of spherical wavelets to detect non-gaussianity in the cmb sky. *Mon.Not.Roy.Astron.Soc*, 336, 2008.

[29] M.R. Nolta, J. Dunkley, R.S. Hill, G. Hinshaw, E. Komatsu, D. Larson, L. Page, D.N. Spergel, C.L. Bennett, B. Gold, N. Jarosik, N. Odegard, J.L. Weiland, E. Wollack, M. Halpern, A. Kogut, M. Limon, S.S. Meyer, G.S. Tucker, and E.L. Wright. Five-year wilkinson microwave anisotropy probe observations:angular power spectra. *astro-ph*, 0803.0593, 2008.

[30] A.A. Penzias and R.W. Wilson. A measurement of excess antenna temperature at 4080 mc/s. *ApJ*, 142, 1965.

[31] K.F. Riley, M.P. Hobson, and S.J. Bence. *Mathematical methods for physics and engineering, 2nd edition*. University Press, Cambridge, 2002.

[32] David Schlegel, Douglas Finkbeiner, and Marc Davis. Application of sfd dust maps to galaxy counts and cmb experiments. *astro-ph*, 9809230, 1998.

[33] M. Tegmark, A. de Oliveira-Costa, and A.J.S. Hamilton. A high resolution foreground cleaned cmb map from wmap. *Phys.Rev*, 68, 2003.

[34] V.M.Slipher. Spectrographic observations of nebulae. *Popular Astronomy*, 23, 1915.

[35] R.A. Watson, R. Rebolo, J.A. Rubino-Martin, S. Hildebrandt, C.M. Gutierrez, S. Fernandez-Cerezo, R.J. Hoyland, and E. S. Battistelli. Detection of anomalous microwave emission in the perseus molecular cloud with the cosmosomas experiment. *ApJ*, 624, 2005.

[36] Eric W. Weisstein. Normal distribution. From MathWorld–A Wolfram Web Resource., 1996. http://mathworld.wolfram.com/NormalDistribution.html.